Intersensor Calibration of DMSP SSM/I's: F-8 to F-14, 1987–1997

Marie C. Colton, *Associate Member, IEEE*, and Gene A. Poe, *Member, IEEE*

***Abstract*— The Defense Meteorological Satellite Program (DMSP) operational special sensor microwave imager (SSM/I) marked its ten-year anniversary on the launch date of the first SSM/I (F-8), June 19, 1997. After F-8, the DMSP has launched five more SSM/I's, F-10 (December 1990), F-11 (November 1991), F-12 (August 1994), F-13 (March 1995), and F-14 (April 1997), leaving the last SSM/I for a candidate launch in 1999. Built by Hughes Aircraft Co., these instruments have proven to be the most reliable and well-calibrated, space-based, passive microwave imaging radiometers to date, allowing the data to be used quantitatively for both operational and climatological applications.**

The remarkable stability of the SSM/I sensors also provides the opportunity to quantify the incremental brightness temperature differences to which the SSM/I's can be intercalibrated, thus establishing the "noise floor" for intercomparisons. This paper summarizes the prelaunch and postlaunch performances of each new sensor determined during calibration and validation (cal/val), starting with the formal, multiyear cal/val effort conducted by both government and public institutions under the direction of the Naval Research Laboratory (NRL) and sponsored by the joint Air Force/Navy DMSP. Sensor-specific components, orbital configuration, and systematic relative errors are examined that contribute to the total system calibration. In particular, a large (1–3 K) but correctable left–right scan asymmetry of SSM/I brightness temperatures was observed in the data and traced to an antenna field-of-view (FOV) intrusion by the spacecraft (start of scan) and a glare suppression sensor (end of scan). These effects were found to be correctable to first order using a pixel-dependent spillover correction. Empirical statistical distribution functions for rain-free ocean pixels were constructed for the entire set of SSM/I's and formed the basis for assessing intersensor calibration. Manufacturer-derived sensor-specific antenna pattern correction (APC) coefficients were found to be the source of large intersensor differences for several channels, e.g., 1–2 K for the 22-V channel. These differences were dramatically reduced when analyzed on the basis of the temperature data record (TDR), i.e., prior to application of the APC, suggesting that studies requiring high intersensor accuracy should use a single set of APC coefficients.

The statistical analyses have obvious inherent limitations themselves. The results of this study indicate that the "noise floor" to which we can justifiably compare individual SSM/I sensors is approximately 0.3 K, depending on the channel, and is a combination of actual sensor calibration differences and the comparison methodology.

Manuscript received April 22, 1997; revised February 17, 1998. This work was supported by the Navy Space and Warfare Command Contract [Nooo3997WXDF524, CDR L. Burgess (retired) and CDR T. Sheridan] and DMSP System Program Office (N000CI73700173, Capt. M. Murphy).

M. C. Colton was with the Satellite Division, Fleet Numerical Meteorology and Oceanography Center, Monterey, CA, 93943 USA. She is now with the Office of Naval Research, Arlington, VA 22217 USA (e-mail: coltonm@onr.navy.mil).

G. A. Poe is with the Naval Research Laboratory, Washington, DC 20375 USA.

Publisher Item Identifier S 0196-2892(99)00038-8.

***Index Terms*— Brightness temperature comparisons, Defense Meteorological Satellite Program (DMSP) special sensor microwave/imager (SSM/I), microwave radiometry, satellite radiometer calibration and validation, sea surface wind.**

I. Introduction

A FORMAL, multiyear calibration and validation (cal/val) effort was initiated with the launch of the first joint Air Force/Navy Defense Meteorological Satellite Program (DMSP) Special Sensor Microwave/Imager (SSM/I) in July 1987. Conducted by both government and public institutions under the direction of the Naval Research Laboratory and the sponsorship of the DMSP System Program Office, the objectives of the postlaunch SSM/I studies were to establish the absolute calibration and sensitivity of the instrument, determine its geolocation accuracy, validate the prelaunch geophysical algorithms using on-orbit data, and implement algorithm changes if needed to meet instrument specification. The results of these first cal/val studies were documented in a series of reports and journal articles ([1]–[3]). The recommended sensor parameter corrections and environmental algorithm changes were applied in stages from 1989 to 1991 to the operational SSM/I ground processing software installed at the Fleet Numerical Meteorology and Oceanography Center (FNMOC) and Air Force Global Weather Central (AFGWC) [4].

Less well known is the fact that the DMSP System Program Office has continued to support similar, albeit less formal, cal/val efforts on each SSM/I, prior to public release of data from each new sensor ([5]–[9]). Evolving from procedures developed at the Naval Research Laboratory, a 30-day Early Orbit Period calibration is now conducted in real time at FNMOC to expedite release of data for operational use. Sensor health is then continuously monitored after this period for the lifetime of the instrument. The SSM/I's have individually proven to be remarkably reliable and stable sensors.

Now that six of the seven existing SSM/I's have been launched (Table I), creating a continuous, decadal, satellite microwave radiometer record, many researchers are analyzing the brightness temperature data for long-term climate change applications, improvement of the geophysical algorithms, and direct data assimilation into numerical weather prediction models ([10]–[22]). These investigations have a common problem, namely, how to obtain continuous environmental data records that are independent of, or transparent to, the specific SSM/I sensor measurements.

In several instances, *ad hoc,* "sensor" corrections (slopes and offsets) have been constructed through statistical regres-

TABLE I
DMSP ON-ORBIT SSM/I SUMMARY INFORMATION (1995)

	F8	F10[1]	F11	F12[2]	F13	F14[3]
Longitude of ascending node (0Z rev)	94.4	-28.5	-84.9	-38.8	-94.4	-53.90
Period (min)	101.74	100.52	101.85	101.94	101.93	101.91
Eccentricity	0.00143	0.00793	0.00129	0.00126	0.00072	.00089
Semi-major - Semi-minor (m)	7.8	225.5	6.0	5.7	2.0	3.0
Focal Distance (km)	10.3	56.8	9.3	9.1	5.2	6.4
Altitude (km)	835-872	726-861	836-876	841-881	845-877	855-861
Mean Earth Incidence Angle (deg)[4]	53.04	53.14	53.29	53.32	52.94	53.25
Precession of perigee (deg/day)	-2.8	-3.0	-2.8	-2.8	-2.8	-2.8
Local Time Ascending Node	0630	2045	1710	2045	1735	2040
Launch Date	19Jun87	1Dec90	28Nov91	29Aug94	24Mar95	4Apr97

[1] Turned off November 14, 1997.

[2] F12 SSM/I failed December, 1994.

[3] F14 Early Orbit Period from power-up, orbit #75, 9 Apr 97

[4] Monthly mean with sensor alignment coefficients applied (Table VI), within +/-60 deg latitude.

sion to address the apparent systematic differences observed between the individual SSM/I data sets. However, it should be noted that regardless of how useful these corrections may be, care must be exercised when attempting to interpret these corrections in terms of real sensor-to-sensor differences, i.e., cross-calibration differences. That is, the observed brightness temperature differences may be attributed to differences of the earth incidence angles (associated with sensor-to-spacecraft alignment offsets and spacecraft orbital differences), misalignments of the antenna beam centers and antenna gain functions (e.g., misalignments of the elliptical beam patterns), or atmospheric and surface inhomogeneities and anisotropies.

Clearly, multisensor comparisons that attempt to interpret deci-Kelvin brightness temperatures require knowledge of real instrument drifts or systematic differences between sensors and the "system error bars" of the naturally occurring incremental temperature differences between sensors, beyond which any two sensors can be statistically compared. To this end, a detailed examination of SSM/I laboratory calibration data (collected by the instrument manufacturer, Hughes Aircraft Co.) and SSM/I orbital data collected over a large time period and of a reasonably stable target are needed to establish these limits and, if possible, identify areas where the level of comparisons may be extended through improved sensor design and performance characterizations.

In this paper, we provide laboratory measurements pertinent to the on-orbit performance of each individual instrument taken during thermal vacuum radiometer calibration and antenna range tests of the reflector and feedhorn subsystems, and then we summarize the corresponding on-orbit results from each Early Orbit Period (Section II). Methodologies for comparing the intersensor data are described next, from which dependencies of the statistical distribution of the measured brightness temperatures on environmental or instrumental parameters can be examined (Section III). We note that corrections or interpretations based on a single average temperature for each channel are not necessarily representative of the entire range of brightness temperatures for that channel. Therefore, in Section IV, we examine annual distribution functions of brightness temperature of rain-free pixels over the open ocean to characterize the overall variations between sensors. We offer guidance on how these differences should be interpreted and the associated implications with respect to improved retrieval methods and forward modeling of brightness temperatures in Section V.

II. PREFLIGHT AND EARLY ORBIT ANALYSES

The original requirements for the SSM/I were specified in terms of the desired accuracies of the retrieved environmental parameters, as summarized in [1]. Therefore, instrument performance requirements for the channel frequencies and polarization, bandwidth, radiometric sensitivity, antenna beam parameters, and the absolute radiometer calibration methodology were "derived" from analyses of the geophysical retrieval algorithms for each of the parameters. In this way, Hughes Aircraft Co. imposed absolute radiometric calibration for each channel to be better than 1.5 K and the required radiometer sensitivities of the channels to be better than 0.8 K for 19 and 22 GHz, 0.6 for 37 GHz, and 1.1 K for 85 GHz.

The calibrated effective blackbody temperature of the radiance incident on the antenna reflector is referred to as the sensor data record (SDR) in the ground processing software. Since the SSM/I is periodically calibrated at the input to the feedhorn, it is convenient to define an intermediate parameter, the temperature data record (TDR), as the effective blackbody temperature of the radiance input to the feedhorn. Five radiometric samples of the warm-load calibration target ($\overline{V}_{WL}$) and cold space observations ($\overline{V}_C$) are averaged for each scan along with the average of three precision thermometric measurements ($\overline{T}_{WL}$) of the warm-load target to establish the TDR (T_A) associated with the scene radiometric measurement (V_A)

$$T_A = \left(\frac{\overline{T}_{WL} - T_C}{\overline{V}_{WL} - \overline{V}_C}\right)(V_A - \overline{V}_C) + T_C \qquad (1)$$

where T_C is the effective cosmic background temperature. A slight improvement in (1) can be obtained to extend the averages to include multiple scans of data, e.g., ten scans of calibration data are averaged in the operational SSM/I ground processing software.

The transformation of TDR's to SDR's occurs through the antenna pattern correction (APC), which attempts to correct for incomplete radiometric coupling between the reflector and feedhorn and cross-polarization coupling between channels and sidelobe contamination. Due to relatively high SSM/I antenna main-beam efficiencies, first-order correction for these

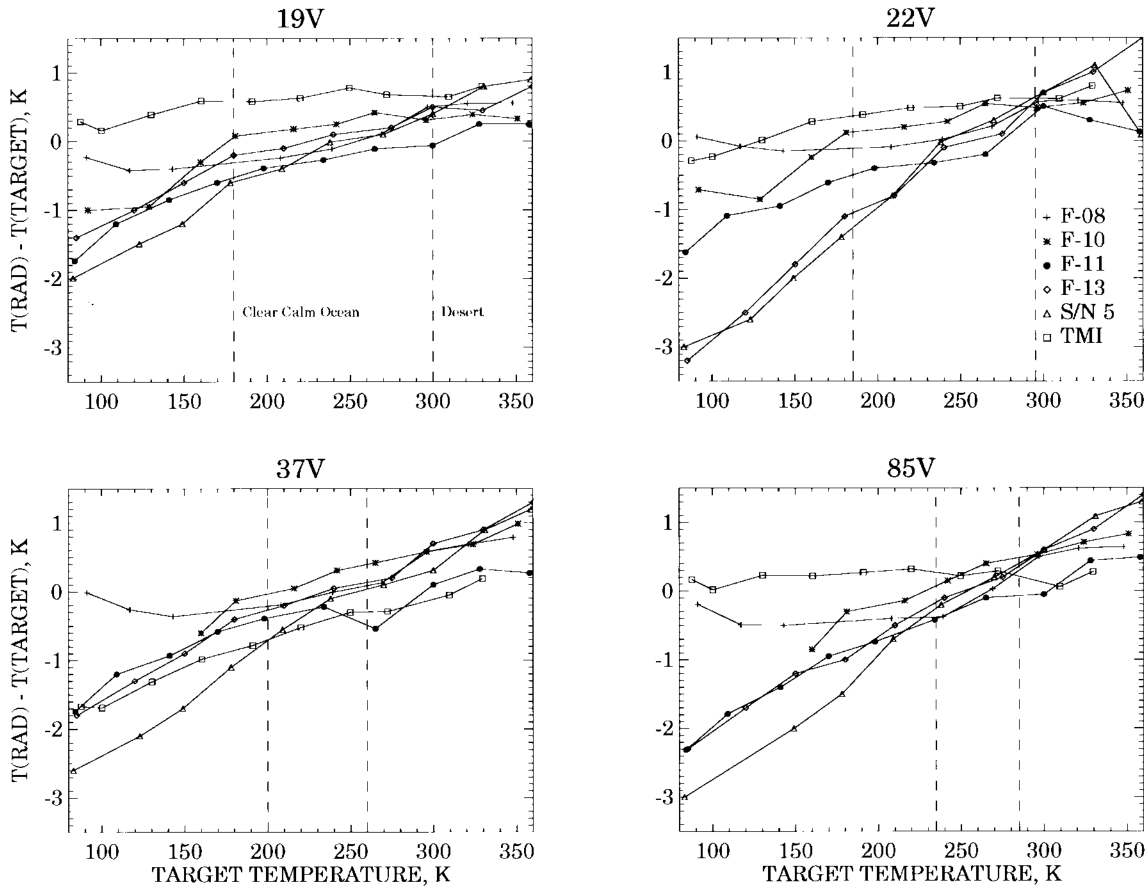

Fig. 1. Prelaunch thermal vacuum calibration results for DMSP SSM/I's F08, F10, F11, F13, F14 (S/N 5), and TMI, vertically polarized channels. Dashed vertical lines denote nominal on-orbit operating range of temperatures showing that, within this range, the SSM/I's meet calibration specifications of approximately 1 K for all frequencies.

effects may be expressed as

$$T_{B_p} = c_0 T_{A_p}(n) + c_1 T_{A_q}(n) + c_2 T_{A_p}(n-1) + c_3 T_{A_p}(n+1) \quad (2)$$

for $p = V$ (vertical), H (horizontal), and $q = H, V$. $T_{Ap}(n)$ are the TDR's of the nth scene of polarization p, and $T_{Aq}(n)$ is the cross-polarized TDR of the nth scene; $T_{Ap}(n-1)$ and $T_{Ap}(n+1)$ are the copolarized antenna temperatures of the adjacent along-scan scenes, and c_i denote APC coefficients established from analyses of antenna range measurements. (The cross-polarized 22-GHz TDR channel is estimated from the horizontally polarized 19-GHz channel $T_{22H} = 0.653 T_{19H} + 96.6$). Due to the small magnitudes of c_2 and c_3, and the fact that $T_{Ap}(n) \approx T_{Ap}(n-1) \approx T_{Ap}(n+1)$, a simplification may be made to (2) by combining c_2 and c_3 into c_0. That is, letting $c_0' = c_0 + c_1 + c_3$ then

$$T_{Bp}(n) = c_0' T_{Ap}(n) + c_1' T_{Aq}(n). \quad (3)$$

This reduced form of the APC agrees with (1) to within 0.1–0.2 K over open ocean scenes, permits computation of the scan edges since only the scene of interest is needed, and allows a one-to-one transformation between TDR's and SDR's. Therefore, we have adopted the simplified APC for all results presented herein.

Due to prohibitive engineering, risk, and costs of an end-to-end prelaunch radiometric calibration (from the energy incident on the antenna reflector through the radiometers to the digitized output), the DMSP initiated a cal/val program once the SSM/I was functioning as a complete system on-orbit. Therefore, it becomes imperative to carefully calibrate each subsystem on the ground, verifying its conformance to requirements, with the final system calibration established on-orbit.

A. Preflight Measurements of the Radiometer and Antenna Subsystems

To demonstrate that the radiometer absolute calibrations of the TDR's are within specification for a range of predicted orbital conditions prior to launch requires replacing the cosmic background with a cold target in the thermal vacuum test setup: in the case of the SSM/I, a liquid nitrogen target cooled to about 80 K. A wide range of earth scene measurements were modeled using a second target of identical construction with variable temperature. Calibration cycles were run for the cases of cold, ambient, and hot canister temperatures to provide the full range of expected instrument temperatures.

For a warm load temperature of approximately 280 K, variable target temperatures ranging from approximately 80 to 330 K and holding the instrument temperature at am-

TABLE II
ANTENNA PATTERN CHARACTERISTICS: (a) VERTICAL POLARIZATION AND (b) HORIZONTAL POLARIZATION

CH	S/C	BW	XP	SO	BE	C0	C1	C2	C3
19V	F-08	1.87	0.47	3.1	95.2	1.04710	0.00490	0.00730	0.00290
	F-10	1.85	0.41	3.1	95.5	1.04570	0.00430	0.00550	0.00390
	F-11	1.87	0.39	3.1	95.3	1.04100	0.00410	0.00283	0.00208
	F-12	1.89	0.61	3.1	95.2	1.04780	0.00640	0.00550	0.00390
	F-13	1.87	0.55	3.1	95.0	1.04328	0.00573	0.00321	0.00234
	F-14	1.88	0.52	3.3	94.9	1.0480	0.00547	0.00524	0.00325
	S/N6	1.86	0.62	3.4	94.6	1.04785	0.00645	0.00354	0.00265
22V	F-08	1.60	1.06	2.6	94.8	1.0513	0.0111	0.00800	0.00550
	F-10	1.60	0.69	2.6	94.7	1.04510	0.00720	0.00600	0.00520
	F-11	1.59	0.70	3.1	94.0	1.04511	0.00735	0.00323	0.00255
	F-12	1.63	1.00	2.6	94.9	1.04750	0.01050	0.00750	0.00290
	F-13	1.59	0.53	3.3	94.2	1.04489	0.00549	0.00245	0.00280
	F-14	1.60	0.66	3.5	93.8	1.05228	0.00691	0.00423	0.00486
	S/N6	1.60	0.51	3.3	95.0	1.04606	0.00533	0.00340	0.00321
37V	F-08	1.05	2.11	1.4	93.5	1.0422	0.02250	0.00320	0.0022
	F-10	1.12	2.30	1.4	94.4	1.04070	0.02440	0.00100	0.00100
	F-11	1.01	1.96	1.3	92.2	1.03622	0.02067	0.00131	0.00111
	F-12	0.93	2.53	1.4	89.3	1.04600	0.02700	0.00030	0.00460
	F-13	1.02	1.98	1.6	91.8	1.03910	0.02097	0.00091	0.00098
	F-14	1.03	1.93	1.8	92.4	1.04102	0.02037	0.00111	0.00119
	S/N6	1.03	1.44	1.8	92.9	1.03626	0.01505	0.00176	0.00111
85V	F-08	0.44	1.36	1.2	91.3	1.0341	0.01420	0.00400	0.00370
	F-10	0.43	2.22	1.2	91.5	1.04820	0.02360	0.00830	0.00410
	F-11	0.46	2.57	1.1	91.6	1.04042	0.02734	0.00104	0.00098
	F-12	0.44	2.65	1.2	91.8	1.05170	0.02880	0.00610	0.00470
	F-13	0.46	2.68	1.1	89.6	1.04292	0.02810	0.00182	0.00182
	F-14	0.45	2.24	1.2	89.6	1.03905	0.02351	0.00172	0.00172
	S/N6	0.43	2.73	1.4	89.2	1.04581	0.02887	0.00137	0.00137

(a)

CH	S/C	BW	XP	SO	BE	C	C1	C2	C3
19H	F-08	1.88	0.41	3.1	95.4	1.04720	0.00430	0.00800	0.00280
	F-10	1.89	0.82	3.1	95.3	1.05040	0.00860	0.00730	0.00260
	F-11	1.87	0.37	3.2	95.1	1.04413	0.00381	0.00374	0.00352
	F-12	1.90	0.76	3.1	95.1	1.05000	0.00790	0.00670	0.00340
	F-13	1.89	0.43	3.0	95.2	1.04238	0.00443	0.00358	0.00345
	F-14	1.89	0.42	3.4	94.8	1.04856	0.00452	0.00407	0.00477
	S/N6	1.87	0.42	3.1	94.1	1.04517	0.00444	0.00322	0.00339
37H	F-08	1.06	2.56	1.4	93.2	1.04280	0.02720	0.00100	0.00040
	F-10	1.07	1.94	1.4	94.9	1.03600	0.02050	0.00030	0.00100
	F-11	1.02	1.91	1.5	92.6	1.03948	0.02016	0.00194	0.00211
	F-12	1.08	2.60	1.4	90.1	1.04330	0.02780	0.00030	0.00100
	F-13	1.03	1.78	1.7	92.4	1.03923	0.01876	0.00151	0.00165
	F-14	1.04	1.52	1.7	93.2	1.03716	0.01601	0.00174	0.00214
	S/N6	1.01	1.44	1.8	93.0	1.03669	0.01506	0.00188	0.00142
85H	F-08	0.44	1.92	1.2	89.1	1.03590	0.02010	0.00270	0.00090
	F-10	0.43	2.71	1.2	88.0	1.04940	0.02880	0.00670	0.00180
	F-11	0.46	2.12	1.3	88.4	1.03878	0.02253	0.00152	0.00152
	F-12	0.44	4.04	1.2	87.0	1.06490	0.04380	0.00630	0.00260
	F-13	0.47	1.16	0.9	89.5	1.02474	0.01215	0.00182	0.00172
	F-14	0.45	1.29	1.4	90.8	1.03124	0.01354	0.00174	0.00172
	S/N6	0.44	1.22	1.4	88.3	1.03015	0.01291	0.00152	0.00152

(b)

bient, the differences between the TDR's and the physical target temperature measured by thermistors are shown in Fig. 1. For the on-orbit operating range bounded by cloud-free calm ocean and hot desert, the calibration errors are typically −1.4 to 0.5 K and within instrument specification. The larger negative temperature differences at low target temperatures for F-10–13 were thought to be due to incomplete radiometric coupling between the feedhorn and fixed cold target [31]. Therefore, a shroud was added to the fixed cold target during the thermal vacuum calibration of the Tropical Rainfall Measuring Microwave Imager (TMI), resulting in a more level calibration error curve. These data show that over the operating range, the radiometers were within the derived specification during thermal vacuum tests. (Similar results were obtained for 273-K (cold) and 305-K (hot) canister temperatures.) However, since the measurements are believed to contain artifacts of the actual test setup, Hughes Aircraft Co. and NRL engineers judged that it would be inappropriate to apply these calibration corrections to on-orbit data since the coupling errors between the feedhorn and cold-space mirror was expected to be much smaller than that achieved with the laboratory cold target. (The mirror and feedhorn spillover both view the cosmic background.)

To complete the ground instrument calibration requires a radiometric characterization of the antenna reception properties. The radiometric performance of the SSM/I antenna was established from analyses of the antenna gain function as measured on an antenna range from which the main-beam efficiency, beamwidth, and feedhorn spillover and cross-polarization losses are determined. In particular, the feedhorn spillover loss for a specified channel is estimated by integrating the normalized antenna pattern measurement of the feedhorn over the radio frequency (RF) receiver bandwidth and over the solid angle subtended by the reflector. Cross-polarization losses are determined by integrating the secondary cross-polarization antenna pattern data (i.e., the combined reflector/feedhorn).

The left-hand columns of Table II summarize for each SSM/I the antenna 3-dB beamwidth (BW, average of E and H planes), the percentage cross-polarization energy (XP), the percentage spillover loss (SO), and the main-beam efficiency (BE) prior to performing the APC. The 3-dB beamwidths vary less than 10% between the instruments, and the cross-polarization and spillover losses exhibit variability between instruments. The largest variation of cross polarization occurs in the 85-GHz horizontal polarization channel (F-13, 1.16% to F-12, 4.04%), while the largest variation of spillover loss occurs in the 22-GHz channel (F-8, F-10, 2.6% to F-14, 3.5%). The magnitude of these components is a function of the feedhorn design and manufacturing process, and the positioning and alignment of the feedhorn with respect to the reflector and must be determined from accurate antenna range measurements.

To appreciate the impact of the APC's on the SDR's, Table III shows the effects of sensor-specific APC's for a highly polarized ocean and unpolarized (blackbody) scene at 260 K. The selected TDR's for each channel are shown in the left-hand column, while differences between the corresponding F-8 SDR's and those associated with other SSM/I SDR's define the remaining columns. For the ocean scene, both antenna cross polarization and spillover contribute to the differences shown. Note that relatively large differences occur for the 22-GHz channel between F-8 and F-11 (−1.02 K), F-13 (−1.43 K), F-14 (−1.96 K), and F15 (−1.42 K), which

TABLE III
EFFECT OF SSM/I APC COEFFICIENTS ON BRIGHTNESS TEMPERATURE: (a) HIGHLY POLARIZED SCENE AND (b) BLACKBODY SCENE AT 260 K

Channel	TDR(K)	F8-F10	F8-F11	F8-F12	F8-F13	F8-F14	F8-S/N6
19V	197.0	0.04	0.05	-0.10	-0.05	-0.46	-0.73
19H	131.0	0.31	-0.16	0.25	0.16	-0.39	-0.26
22V	222.0	0.16	-1.02	0.05	-1.43	-1.96	-1.42
37V	213.0	-0.11	0.36	-0.22	-0.32	-0.74	-0.43
37H	155.0	-0.39	-0.57	0.03	-0.97	-1.12	-1.34
85V	258.0	-0.31	-0.14	-0.46	-0.20	-0.28	-1.00
85H	225.0	0.31	-0.15	0.78	0.45	-0.68	-0.69

(a)

Channel	TDR(K)	F8-F10	F8-F11	F8-F12	F8-F13	F8-F14	F8-S/N6
19V	260.0	0.00	0.00	0.00	0.00	-0.55	-0.83
19H	260.0	0.05	-0.25	0.03	0.31	-0.81	-0.53
22V	260.0	-0.02	-1.40	0.02	-1.97	-2.52	-1.97
37V	260.0	0.00	0.30	0.05	-0.50	-1.05	-1.05
37H	260.0	0.00	-0.28	0.00	-0.81	-0.80	-1.07
85V	260.0	0.00	0.30	0.03	0.27	-0.03	-0.52
85H	260.0	0.03	-0.26	0.00	0.82	-0.53	-0.52

(b)

are due primarily to the differences in spillover loss, as seen in Table II. A similar situation occurs for the 37-H channels.

For the unpolarized scene at 260 K [Table III(b)], the spillover is the only factor that contributes to the differences and the effect is magnified due to the increased TDR. At 22 GHz, the differences approach 2 K between F-8 and F-13 and 2.5 K between F-8 and F-14. Although not shown, relatively small differences occur between the F-8 APC and the APC used by Wentz for F-8 [23].

The accuracy of the APC coefficients is a function of the number of antenna range measurements (i.e., elevation and azimuthal cut increments across the channel passband), the dynamic range of the antenna measurements (i.e., the noise floor of the range), and the repeatability, accuracy, and stability of the antenna range transmitter/receiver over the period of observation. Based on discussions with the manufacturer, we estimate that the feedhorn spillover efficiency has an absolute accuracy of 0.3–0.5%, while the cross-polarization relative accuracy is of the order of 5–10%. The uncertainty in the spillover measurement error translates to 0.9–1.5 K for a 300-K scene, while the cross-polarization error is about 0.15–0.3 K for a 50-K scene polarization (assuming a 3% cross-polarization coupling). In view of the magnitudes of these potential errors, both the TDR (pre-APC) and SDR (post-APC) brightness temperatures are retained in the subsequent intersensor comparisons.

The antenna range measurements also establish the electrical boresights of the antenna beams (i.e., centroid of the energy) in terms of the mechanical boresight. Due to the aforementioned performance difference in feedhorns and their respective alignment errors with the reflector, the electrical boresights vary slightly between instruments (typically -0.05 to $0.23°$) and are included in the pixel geolocation determination. The variation of boresights between channels for a given instrument is less than 0.05°. The elevation offset due to reflector deployment varies between instruments, typically -0.37 to 0.25°, and is included in the geolocation and earth incidence angle computations.

TABLE IV
SSM/I WARM-LOAD NOISE EQUIVALENT TEMPERATURE DIFFERENCE

Channel	F-8	F-10	F-11	F-12[1]	F-13	F-14[2]	Spec.
19V	0.37	0.50	0.46	0.48	0.49	0.44	0.8
19H	0.37	0.48	0.39	0.42	0.40	0.49	0.8
22V	0.58	0.54	0.55	0.62	0.55	0.61	0.8
37V	0.30	0.37	0.34	0.31	0.34	0.31	0.6
37H	0.33	0.37	0.35	0.31	0.32	0.35	0.6
85V	0.69	0.53	0.58	0.62	0.48	0.54	1.1
85H	0.59	0.57	0.44	0.56	0.49	0.48	1.1

[1] F12 SSM/I failed December, 1994. Values listed apply to 30 day Early Orbit Period.

[2] F14 Early Orbit Period from power-up, orbit #75, 9-16 April, 1997.

B. On-Orbit Sensor Evaluation

In the 30-day orbital period following each sensor deployment and power-up (nominally 77 orbits after launch), the radiometer gain, sensitivity (Table IV), and temperature stability of all channels are monitored, quantified, and validated in terms of instrument specifications. In addition, analyses are conducted of calibration samples for uniformity and stability and of the quality of the imaging across the swaths. Cross calibrations between previous operational SSM/I's are made for a wide range of surface types. Evaluations of the geolocation accuracy of the imagery are performed and, if necessary, corrections are generated for the pitch, roll, and yaw coefficients to bring the errors to within 6–7 km (half of the 3-dB beamwidth diameter at 85 GHz). Brief summaries of the major results of these activities are presented below as well as a validation study of the earth incidence angle.

1) Uniformity Across the Swath: The first detailed early orbit assessment of the uniformity of the SSM/I pixels across the swath was undertaken for F-12 and F-13. The means and standard deviations of the absolute brightness temperatures of the ocean between ±60° (as determined by a static surface type data base) were computed at each beam position, minimizing conditions of precipitation by imposing the rain flags developed by Stogryn [24]; i.e., data are accepted that

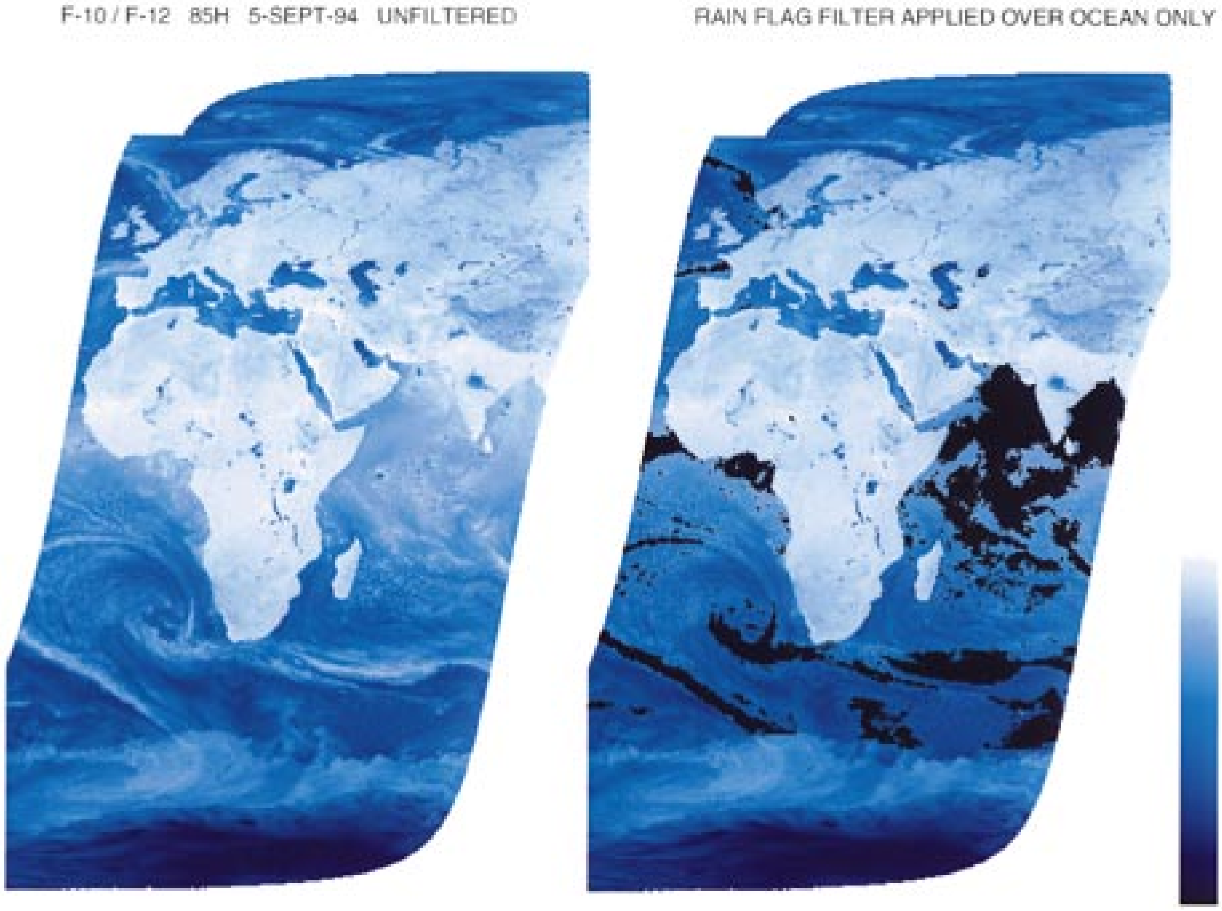

Fig. 2. F10 and F12 composite image, September 5, 1994. Left: all data points. Right: data points filtered as rain contaminated are blacked out. Note the superlative, contiguous coverage of F10 and F12 at the equator that occurred with these two satellites.

pass the tests ($T_{37\,\mathrm{V}} - T_{37\,\mathrm{H}} > 50$; $T_{19\,\mathrm{V}} < T_{37\ \mathrm{V}}$; $T_{19\,\mathrm{H}} < 185$; and $T_{37\,\mathrm{H}} < 210$). The filter rejects approximately 18% of ocean scenes, of which >99% fail the first test. In addition, pixels within 75 km of coastlines were rejected; ascending and descending passes were treated separately. The effect of the rain flag filtering is illustrated as dark areas in the composite image of F-10 and F-12 (Fig. 2).

Although the SSM/I beam samples exhibit a high degree of uniformity across the swath, an expanded view of the variations revealed noticeable deviations at the scan edges. A rapid fall-off of nearly 1.5–2 K near the end of scan was observed for all channels for F-12 and F-13 SSM/I's for the 30-day Early Orbit Period. This anomalous behavior was first noted by Wentz [25] and attributed to possible field-of-view (FOV) intrusions by the cold space mirror. To determine whether this behavior was also present in larger data sets, the means and standard deviations of monthly averaged, rain-free brightness temperatures for each beam position and ascending/descending passes were initiated with early orbit cal/val of F-13.

The deviations of the annual mean brightness temperature (including ascending and descending passes) for each pixel from the average of the 20 (at 19, 22, 37 GHz) and 40 (85 GHz) apparently uncontaminated mid-scan pixels are shown in Fig. 3. The rapid fall-off in brightness temperature is highly correlated, but different, among channels and all SSM/I's. The largest fall-off occurs at 22- and 85-GHz, vertical polarization and reaches 2–4 K. This behavior was observed to be systematic and slightly different for both ascending and descending annual and monthly averages. Note also a small, but discernible fall-off at the beginning of the scan as well.

To determine if there was an engineering explanation for this behavior, the authors contacted the spacecraft manufacturer and sensor integrator (Lockheed-Martin, Princeton, NJ) for information about possible intrusions by the spacecraft or other payloads into the SSM/I FOV, especially at the end of scan. The SSM/I Interface Control Document ([26], courtesy of Dr. R. Churi, Lockheed Martin) indicated that there was a known intrusion near the end of the scan by the glare Suppression System-B (GSS-B) (Fig. 4). The surface of the GSS-B is composed of aluminized teflon and would appear as a highly reflective surface at microwave frequencies. The surface geometry of the GSS-B is oriented so that primarily only incoming 3-K cosmic background energy is scattered into the SSM/I FOV. More importantly, the FOV intrusion reduces the upwelling scene radiance received by the feedhorn. From Fig. 4, it also appears possible that the fall-off at the beginning of the scan may be due to far sidelobe energy viewing the reflective spacecraft surface.

To first order, the effects of the FOV intrusions can be treated as a beam-position-dependent energy loss. The correction procedure that would be applied in the operational

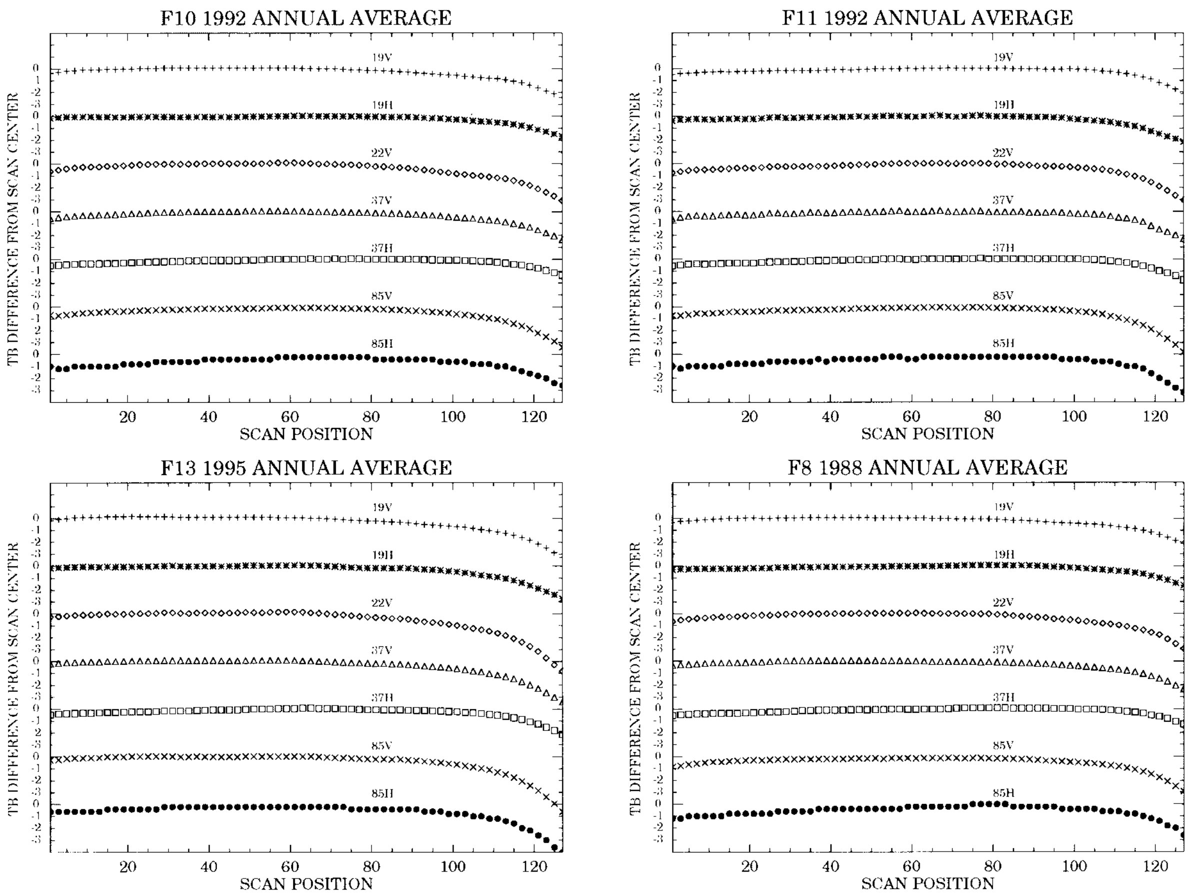

Fig. 3. Typical plots for F8, F10, F11, and F13 of the annual averaged brightness temperature deviations from beam-center mean as a function of beam position. The low-frequency pixels have been registered to odd-numbered 85-GHz pixels, and only those pixels containing all frequencies are included. The even-numbered 85-GHz pixels exhibited the same behavior as the odd numbered.

Fig. 4. Top view of SSM/I at the first active beam position, integrated on DMSP spacecraft. SSM/I scans clockwise and approaches GSS-B, to the lower right of the SSM/I reflector, at the edge of scan.

processing software consists of multiplying the APC coefficients by a pixel-dependent factor, defined as unity plus the ratio of the deviations at each beam position normalized to the average brightness temperature of the central uncontaminated beam positions.

To verify the anomalous along-scan variation may be removed with an equivalent spillover correction in the APC, retrieved sea surface wind speeds were compared to actual buoy observations at each beam position for the cases with and without the along-scan correction. For this task, an extensive

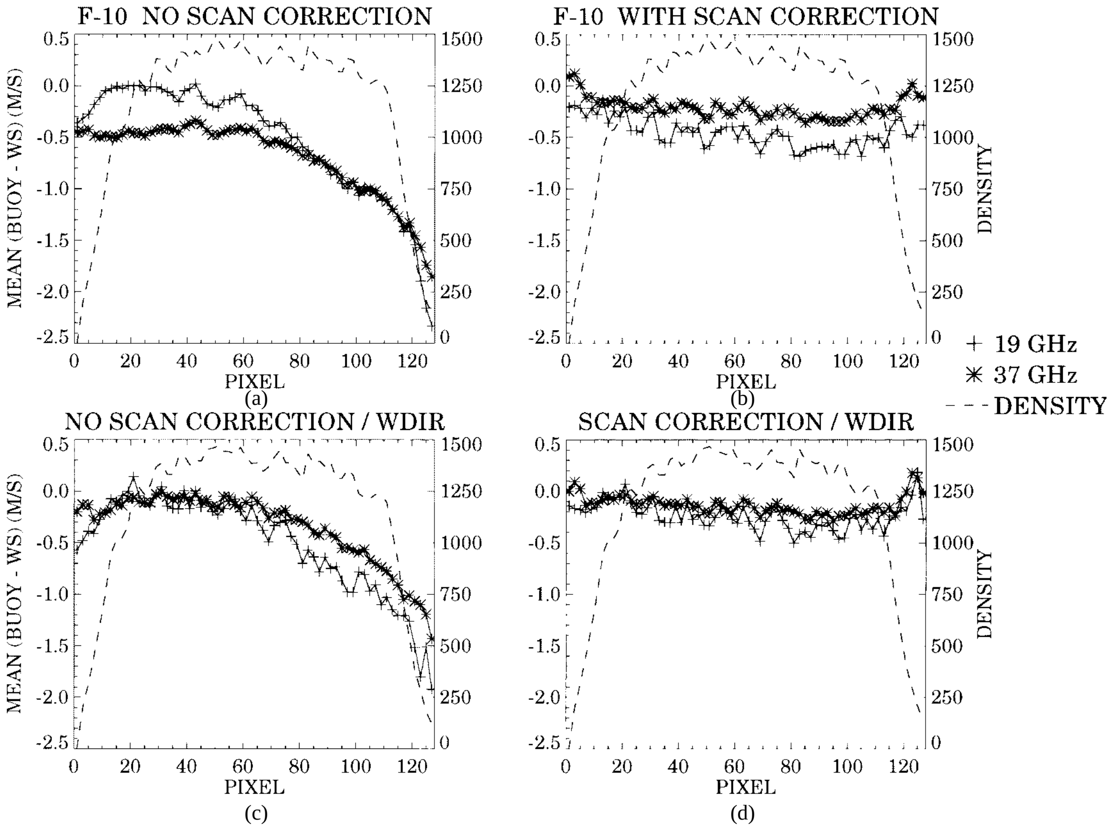

Fig. 5. Mean difference between buoy and SSM/I wind speed measurement for F10 SSM/I, September 1991 to June 1993, and all of 1995, before (a) and after (b) along-scan correction; before (c) and after (d) along-scan correction and including wind direction effect. Similar results were obtained for F11 and F13.

ground truth database was compiled that consists of NOAA and TOGA COARE buoy wind speed measurements interpolated in time to the coincident SSM/I data, within 30 km and 30 min. The matchup periods were 1988–1992 for F-8, 1991–1996 for F-10, 1992–1996 for F-11, and 1995–1996 for F-13. The number of distinct buoy observations passing quality checks were 11381, 18248, 14590, and 9606 for F-8, F-10, F-11, and F-13, respectively, which in turn produced a total number of SSM/I-buoy matchups of 44948, 77351, 58679, and 38 751 for F-8, F-10, F-11, and F-13.

The Wentz [27] 37-GHz algorithms[1] were used to retrieve neutral wind speeds at 19.5 m (corresponding to the buoy wind speed reports) and atmospheric transmissivity since the single-channel algorithms restrict our attention to only these channels during the along-scan comparisons. (This is not strictly correct since the 22-GHz channel is used in conjunction with the 37-GHz wind speed and transmissivity to retrieve cloud liquid water that is used to filter rain. No wind speed retrieval was kept if the cloud liquid water exceeded 0.18 mm, as recommended by Wentz). In addition, using the model functions developed by Wentz, we retrieved windspeeds using the 19-GHz channels and the same cloud liquid water filter noted.

The "bias error," defined as the mean difference between the buoy and retrieved windspeeds, was computed for each pixel with and without the along-scan correction. The increase in the bias error in Fig. 5(a) occurs toward the end of the scan without the correction, while Fig. 5(b), which includes the along-scan correction, removes essentially all of the anomalous behavior. The number of observations per pixel, shown with the right-hand scale, is relatively constant over most of the scan but declines rapidly near the beginning and end of scan, reducing the confidence of the statistics when the number falls below 100 per pixel.

To demonstrate that the along-scan variation is definitely sensor related and not the result of a directional, environmental phenomenon, such as ocean wind direction, the wind speed retrieval algorithm was modified in accordance with the empirical wind direction model of Wentz [27] and the buoy wind direction measurements. Fig. 5(c) and (d) present the bias error as a function of pixel position before and after applying the scan correction. Although the magnitude of the bias errors have changed from Fig. 5(a) and (b), the anomalous scan behavior is again removed with the scan correction. Note that the effect of the GSS-B FOV intrusion on the wind speed retrieval error is more visible when presented in terms of the mean error rather than rms error because the peak-to-peak fluctuations of the wind speed differences are on the order of $\pm$4.5 m/s at 37 GHz and $\pm$6 m/s at 19 GHz, considerably larger than the systematic error introduced by the scan behavior. Consequently, the rms wind speed error does not exhibit the same level of improvement as the mean error after the scan correction is applied.

2) Sensor Differences Between F-8, F-10, and F-11: Prior to the F-12 early orbit cal/val, the relative radiometer cal-

[1]The F-8 model function offsets (2.0 K for 19 V; 3.5 K for 19 H; 1.3 K for 22 V; $-$1.6 K for 37 V, and $-$0.2 K for 37 H) derived by Wentz were retained for other SSM/I's.

TABLE V
SUMMARY OF F10/F8 BRIGHTNESS TEMPERATURE COMPARISONS

Area	19V	19H	22V	37V	37H	85V**	85H**
Amazon (14 passes)	0.5 (0.5)	0.3 (0.6)	-0.2 (0.3)	1.3 (0.7)	0.9 (0.5)	0.4 (2.3)	-0.9 (2.3)
Arabian Desert (10 passes)	-0.1 (1.3)	-0.4 (1.0)	-0.5 (1.0)	0.3 (1.4)	0.0 (1.0)	-1.2 (2.4)	1.3 (3.3)
Greenland (2 passes)	-0.3 (0.2)	-0.8 (0.2)	-0.6 (0.1)	-0.4 (0.5)	-0.8 (0.1)	-1.2 (6.7)	0.1 (6.9)

** Using representative historical values for the F8 85GHz data

(a)

Area	19V	19H	22V	37V	37H	85V	85H
Indian Ocean 54-62S 76-88E	2.1	0.0	1.0	2.0	0.7	---	---
South Pacific 54-65S 184-200E	-0.6	1.1	-1.3	-0.5	1.1	---	---
Eastern USSR 54-62N 41-56E	0.7	0.6	0.3	1.0	0.8	---	---
Central Canada 54-65N 244-254E	0.6	0.9	-0.3	0.8	0.5	---	---
Gulf of Alaska 56-58N 215-221E	-0.8	-0.5	-1.6	-1.1	-1.0	---	---
Hudson Bay 56-68N 272-285E	0.7	0.9	0.1	0.9	0.8	---	---

(b)

ibration accuracies of F-8, F-10, and F-11 were evaluated by comparing the average scene brightness temperatures for a wide range of regions (e.g., Amazon rain forest, Arabian desert, Greenland ice cap, and calm, open ocean with negligible cloud cover). Attempts were made to select data sets that were as close as possible in time, realizing of course that orbital differences would determine the extent that this was achievable. For example, the F-10 and F-8 orbits intersected at times that permitted data comparisons of the selected regions with time differences typically less than 1.6 h. In some instances, near simultaneous (e.g., <3 min) could also be made except at 85 GHz. The situation was more difficult when attempting to compare F-11 and F-10 since the orbits within the 1–2-h window occurred only at high latitudes, above 60°, limiting the range of brightness temperature comparisons.

Table V presents a summary of the differences between F-10 and F-8 brightness temperatures, conducted during the early orbit cal/val. Since the F-8 85-GHz channels were not functioning, representative historical values were used. As seen, the agreement between the absolute calibration of F-8 and F-10 SSM/I's is typically less than 1 K with maximum differences of approximately 2 K. Averaging all comparisons shows that the two SSM/I's agree to within 0.5 K, with an rms scatter of 1 K, except at 85 GHz. Therefore, the conclusion was made that there was no need to adjust the F-10 brightness temperatures or the environmental retrieval algorithm validated for F-8.

A similar set of comparisons were made between F-11 and F-10, albeit with a larger time window due to orbital

TABLE VI
SPIN-AXIS ALIGNMENT COEFFICIENTS AND ELEVATION OFFSETS

DMSP	S/N	El-off prelaunch	Pitch on-orbit	Roll on-orbit	Yaw on-orbit	½ Cone Angle
F-10	1R	-0.37	0.00	0.00	0.10	45.37
F-8	2	0.25	-0.10	-0.10	-0.70	44.85
F-12	3	0.15	0.20	0.10	-0.40	45.05
F-11	4	0.02	0.00	0.00	0.05	44.98
F-13	7	0.05	-0.30	0.00	-0.10	44.65
F-14*	5	0.03	0.00	0.00	-0.65	45.00

* F14, April - June, 1997

differences. Relatively good agreement exists between F-11 and F-10 for all channels, with exception of 22 V, which indicated a potential difference of 1.9 K. Due to the relatively large scatter in the regional comparisons, the differences between the sensor data sets and the orbital differences, no attempt was made to implement a correction for this apparent difference.

3) Geolocation: Evaluation of geolocation accuracy during the F-8 cal/val demonstrated that the onboard ephemeris elements downloaded to the processing centers from the spacecraft should be used in the ground software geolocation computations. The technique used to determine the SSM/I geolocation accuracy consists of visual analyses of the 85-GHz horizontal polarization brightness temperature imagery superimposed with an accurate global shoreline database (Defense Mapping Agency World Vector Shoreline Data Bank II). The accuracy of the DMS shoreline is reported to be better than 1 km over 90% of the all identifiable features.

A set of 12 geographically distributed $20 \times 20°$ latitude/longitude boxes with definite, variable geometry land features are used to detect the presence of geolocation errors. Effective sensor spin-axis attitude adjustments of pitch, roll, and yaw are derived to yield the "best" visual agreement of the 85-GHz imagery in the sense of mean differences and the shoreline database for the ensemble of regions selected. Although an occasional large geolocation error can arise, e.g., when the spacecraft loses attitude control, for normal conditions, incorporation of the spin-axis alignment coefficients reduces the rms geolocation error to less than 4 km, which meets the specification of half the smallest 3-dB beamwidth. It is believed that the error in the pitch correction was usually less than $\sim$4 km, which translates to potential uncertainty in the earth incidence angle of 0.1 deg.

Table VI presents the pitch, roll, and yaw attitude corrections for the SSM/I spin-axis, where positive yaw is defined as right-hand rotation about the local spacecraft zenith; positive roll is defined as right-hand rotation about the spacecraft velocity vector; and positive pitch is defined as right-hand rotation about the orbit normal (the cross product of the velocity vector with the zenith vector). An elevation offset angle (eloff) is determined prior to launch that includes antenna beam boresight and deployment alignment errors (positive eloff is directed toward nadir), which, for completeness, is retained in the ground processing software.

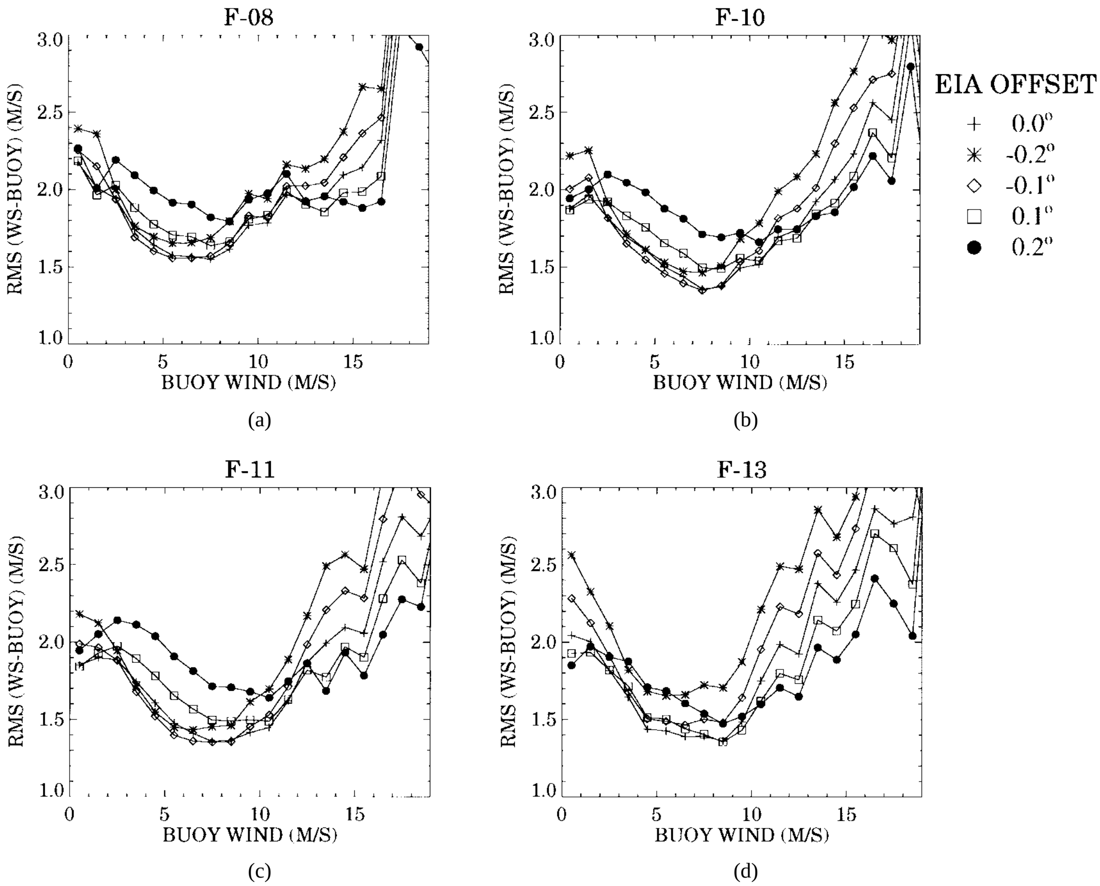

Fig. 6. Rms wind speed retrieval error (including wind direction effect) as a function of buoy wind speed for varying earth incidence angle (EIA) offsets for (a) F8, (b) F10, (c) F11, and (d) F13.

4) Earth Incidence Angle (EIA) Validation: The EIA is a function of the SSM/I orbit eccentricity, the stability of the spacecraft attitude control system, the accuracy of the onboard ephemeris, the oblateness of the earth, the alignment of the electrical beam boresight with the SSM/I coordinates, and the alignment of the SSM/I to the spacecraft. As such, the EIA varies slightly, not only across each scan and within each orbit, but between different SSM/I sensors due to different antenna deployment offsets. The on-orbit geolocation validation procedures outlined above may result in changes to the SSM/I spin axis, which, through the pitch and roll corrections, alters the EIA.

Although direct verification of the true EIA presents a rather formidable task, a partial validation of the EIA values may be obtained by examining the dependence of the rms wind speed retrieval error in terms of different EIA offsets. The database consisted of the SSM/I and buoy matchups discussed above, in conjunction with the Wentz [27] wind speed algorithm, which incorporated the empirical model for wind direction effects. To avoid the effects of different APC coefficients, the F-8 APC was applied to F-10, F-11, and F-13. The distribution of rms wind error as a function of buoy wind for offsets -0.2, -0.1, 0.0, 0.1, and 0.2° (Fig. 6) is smallest in the vicinity of maximum wind speed density, 6–9 m/s. The EIA offsets producing the minima in this wind speed region is approximately $-0.1°$ for F-10 and F-11 and 0.0° for F-13, establishing confidence that the prelaunch beam offsets and the geolocation procedure discussed above yield half-cone angles that are within $\pm 0.1°$ of the true cone-angle.

III. Intersensor Comparisons

A. Intercomparison Methodologies

Outside of the brief set of intersensor comparisons presented in Table V, thus far the characteristics of the sensors have been addressed to specify the level of performance for the individual sensors. In the remaining sections, the objective is to quantify the statistical differences among the sensors and establish the limits of comparisons that can be made between sensors. Typically, sensor comparisons between versions of the same instrument are accomplished by examining pixels from the multiple sensors that are coincident to within specified time and space criteria. This method is frequently adopted during cal/val activities or an algorithm validation study for matching on-orbit data with ground truth observations. However, coincident pixel comparisons have the disadvantages of limited points due to orbital differences, coincident regions that are not uniformly distributed, and errors due to geolocation inaccuracy and azimuthal (look angle) differences.

To improve the global coverage and averaged statistics, and reduce possible azimuthal variations, a second common approach is to bin the sensor data into latitude/longitude boxes for specified time periods, say, monthly averages in 1° boxes

[22]. The disadvantages here for intersensor comparisons are that interpolation errors are introduced, nonuniform numbers of samples per bin occur, and importantly, the measurement geometry of the original data point is lost.

Other long-term studies of microwave data ([28], [29]) use the time series themselves to attempt to eliminate intersensor differences. That is, the time series of each sensor are analyzed to find seasonal oscillations and trends, which are interpreted as the result of natural environmental variability and known, but not fully quantifiable, orbital variations between sensors. The oscillations and trends are subtracted from the time series, and the remaining deviations are averaged and binned as above to aid in further comparisons based on gridded products. This type of analysis is frequently used when evaluating the satellite data in terms of global environmental data acquired by other sensors, output from numerical forecast models, or the historical record.

Often, the aims of the above methods are to produce an expression for intercalibrating all of the individual time series, or develop new retrieval techniques. However, in our endeavor to identify specific sensor differences, we are concerned that removing variability in mean temperatures due to look direction, EIA, pixel identity, and long-term environmental effects through a series of imperfect corrections and binning will obscure, rather than clarify, the actual sensor differences. Therefore, we advocate a "do no harm" approach to the measurements and seek a comparative data analysis method that does not transform the original sensor data prior to making comparisons.

In the analyses below, we have restricted our intersensor comparisons to observations of rain-free, open-ocean scenes to enhance the channel polarization information and minimize the effects of horizontal inhomogeneities. (Early attempts to establish intersensor comparisons for terrain such as rain forest or deserts were abandoned due to relatively large sensor-to-sensor brightness temperature fluctuations and small number of pixels.) Two methods for examining sensor data are employed. First, orbital averaged data as a function of pixel position are computed for rain-free, ocean scenes for both ascending and descending orbits. This technique significantly increases the number of observations used in the statistics, reduces most of the environmental effects, minimizes surface emissivity (azimuthal) variation, and keeps the pixel identifier. However, as is shown, studies of mean differences provide valuable insight into potential intersensor differences, but they do not exploit the full statistical information contained in the range and frequency of observations. Therefore, the characteristic, annual distributions of brightness temperature (and antenna temperatures) are examined to reduce the impact of imperfect knowledge of orbital and environmental effects and provide a better statistical basis for assessing intersensor differences.

B. Orbital Characteristics

Although the SSM/I instruments fly on an extremely stable DMSP spacecraft platform, normal orbit variabilities and long-term drifts of the orbital elements must be included in detailed analyses of SSM/I data and when fine comparisons are made between different SSM/I's. For example, the analysis of rain-filtered daily averages of SSM/I measurements taken of the ocean exhibit an oscillatory behavior for the ascending and descending passes that are highly correlated with the daily average altitude, which, in turn, is a function of the perigee rotation rate. From Table I, the perigee rotates in the orbit plane at a rate of approximately 2.8°/day, which results in a period of about four months. In addition, long-term precession of the orbit plane manifests itself in a variable solar illumination angle to the sensor and scene of interest, which can produce correlations between the mean environment parameters and daily or monthly average SSM/I data. Fortunately, the details of the spacecraft and SSM/I scan geometry (including spin-axis offsets) are available so that variability of the orbital parameters can be readily examined.

An analysis of the DMSP orbits shows that the F-10 and F-11 orbit planes have drifted eastward 42 and 29° since launch while F-8 has drifted 2° eastward, then 1.5° westward to have nearly the same, at-launch longitudinal crossing, and F-13 has drifted eastward only about 1°. The sun-angles (angle between orbit plane and the sun) for all SSM/I's exhibit expected periodic annual variability on the order of 0–33°, with the exception of F-10, which also possesses an eastward long-term drift. The average time per orbit the SSM/I spends in the earth's shadow is typically less than 15–19 min (during the winter months), with the exception of F-10, which always spends time in the shadow and reaches to 33 min per orbit.

The daily average SSM/I ascending EIA oscillates in quadrature with the descending pass. The peak-to-peak daily average incidence angle variation is greatest for F-10 (52.6–53.7°) and smallest for F-13 (52.9–53.0°), and it is attributable to the orbit eccentricity (Table I). The F-8 incidence angle decreased between 1989 and 1992 by approximately 0.1°, which arises from a slow decrease in average orbit altitude. The EIA can also vary across the scan by approximately 0.1°, due to the spin-axis alignment correction and the earth's oblateness.

C. Illustrative Case: 1992 Annual Statistics

Before undertaking detailed annual comparisons of the SSM/I instruments, analyses were conducted to examine the month-to-month variability of the averaged brightness temperatures with the explicit purpose of determining how much of the variability could be explained in terms of recognizable environmental or orbital differences. Using the rain flags developed by Stogryn [24] noted above, monthly averaged brightness temperatures for open ocean pixels were computed for both ascending and descending passes for 1992. Only those pixels lying within ± 10 centered on position 32 for low frequencies and ± 20 on position 64 for 85 GHz were included. The resulting number of observations in the monthly ascending and descending averages varied from 1 to 1.4×10^5 per month for the 19-, 22-, and 37-GHz channels and from 2 to 2.8×10^5 per month for 85 GHz, representing approximately $82 \pm 2\%$ of the total ocean pixels sampled each month. (Averages of scans containing only the 85-GHz data were analyzed separately and found to agree with the averages of

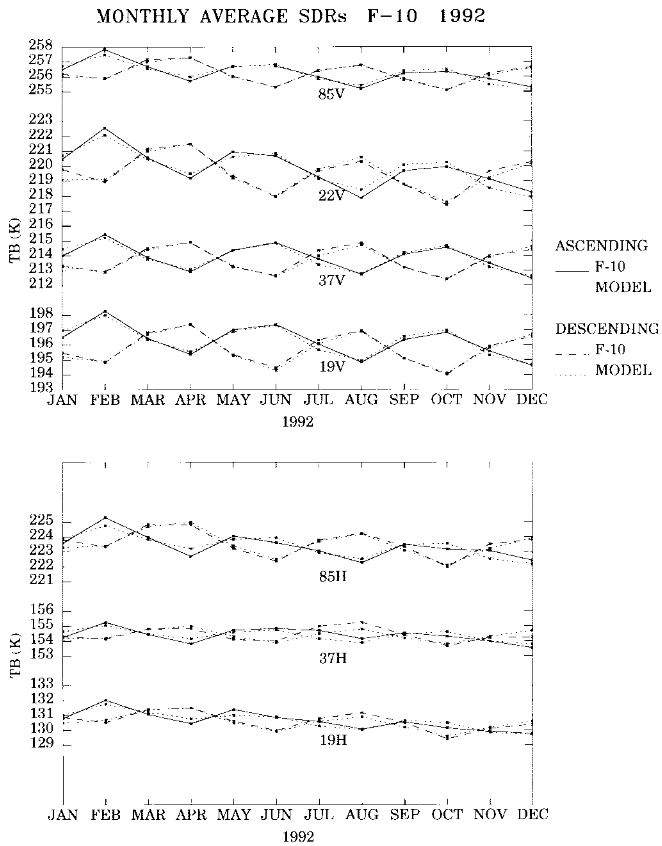

Fig. 7. Monthly averaged, nonprecipitating, ocean SDR's for F10 (with F10 antenna pattern correction) ascending and descending orbits and modeled SDR's superposed, 1992.

TABLE VII
1992 Annual Average and rms Model Errors: (a) F-10, with F-10 APC and (b) F-11, with F-11 APC

	MEAN		RMS Fit of Model	
Channel	Ascending	Descending	Ascending	Descending
19V	196.3	195.8	0.24	0.12
19H	130.6	130.6	0.22	0.19
22V	219.9	219.6	0.37	0.27
37V	213.9	213.7	0.21	0.13
37H	154.4	154.4	0.26	0.26
85V	256.3	256.2	0.22	0.10
85H	223.4	226.3	0.34	0.21

(a)

	MEAN		RMS Fit of Model	
Channel	Ascending	Descending	Ascending	Descending
19V	196.6	196.7	0.14	0.16
19H	130.5	130.7	0.25	0.29
22V	221.7	221.7	0.29	0.33
37V	213.3	214.0	0.17	0.19
37H	153.7	154.8	0.33	0.32
85V	257.3	257.7	0.15	0.19
85H	224.1	225.3	0.34	0.40

(b)

scans containing all channels to within 0.1 K.) Missing data counts were relatively small, less than four, 1/2-day periods were missing for F-10. Occasional "wild" points appeared (two–three per orbit) that were readily identified and removed. Also, random loss of one–two scans per orbit occurred, which does not affect the averages, considering the total number of points. No discernible correlation could be found between the number of pixels passing the rain flag each month and the monthly averaged brightness temperatures.

The monthly averages for the F-10 SDR's exhibit a large oscillatory behavior (Fig. 7) that is strongly correlated with a similar periodicity in the earth incidence angle. In addition, a decreasing trend in the averages is apparent over the course of 1992, which was greatest for 22 V, implying a correlation with atmospheric water vapor. To test this hypothesis, a simple linear model was generated using the monthly averaged F-10 EIA (within $\pm 60°$ latitude) and the monthly-averaged National Climate Data Center, $1 \times 1°$, sea-surface temperature (weighted by the F-10 sampling density and cosine of the latitude) as a surrogate for water vapor

$$\hat{T}_B = \langle T_B \rangle + \left\langle \frac{dT_B}{d\theta} \right\rangle [\theta(m) - \langle \theta \rangle] + \left\langle \frac{dT_B}{dT_{\mathrm{SEA}}} \right\rangle [T_{\mathrm{SEA}}(m) - \langle T_{\mathrm{SEA}} \rangle] \quad (4)$$

where θ and T_{SEA} are the monthly averaged incidence angle and sea surface temperature for month m and $\langle\,\rangle$ denotes the annual average. The coefficients $\langle dT_B/d\theta \rangle$ and $\langle dT_B/dT_{\mathrm{SEA}} \rangle$ and constants $\langle T_B \rangle$, $\langle \theta \rangle$, and $\langle T_{\mathrm{SEA}} \rangle$ are found by minimizing the variance of the difference between the model and the measurements. A comparison of the model and measurements (dotted lines, Fig. 7) shows surprisingly good agreement [Table VII(a)], demonstrating that the majority of the variance in the F-10 monthly averaged brightness temperature has been explained. This result was not affected by choice of either F-10 or F-8 APC. A similar model fit was made to the 1992 F-11 monthly averaged brightness temperature [Table VII(b)] and indicated that the level of agreement was essentially that obtained with F-10, although the oscillatory behavior was greatly reduced due to the more circular orbit of F-11.

D. Monthly Averaged Brightness Temperatures: 1987–1997

Using the data filtering criteria specified in the previous section, monthly averages of both ascending and descending passes were computed for all of the SSM/I data available in the NRL SSM/I archive, July 1987–December 1997, exclusive of a data gap from September 1993–March 19 95.[2] From Table I, we note that there are small differences in the mean EIA among the sensors that would result in biases when comparing the monthly averages on a single plot. Therefore, for the purpose

[2] The data gap occurred when the SSM/I archival data stream was switched from FNMOC tape transfer to NRL then to NESDIS to direct electronic transfer from FNMOC to NOAA/NESDIS. For data cost/recovery reasons, the direct transfer of archived TDR's from FNMOC to NRL was restored in April 1995.

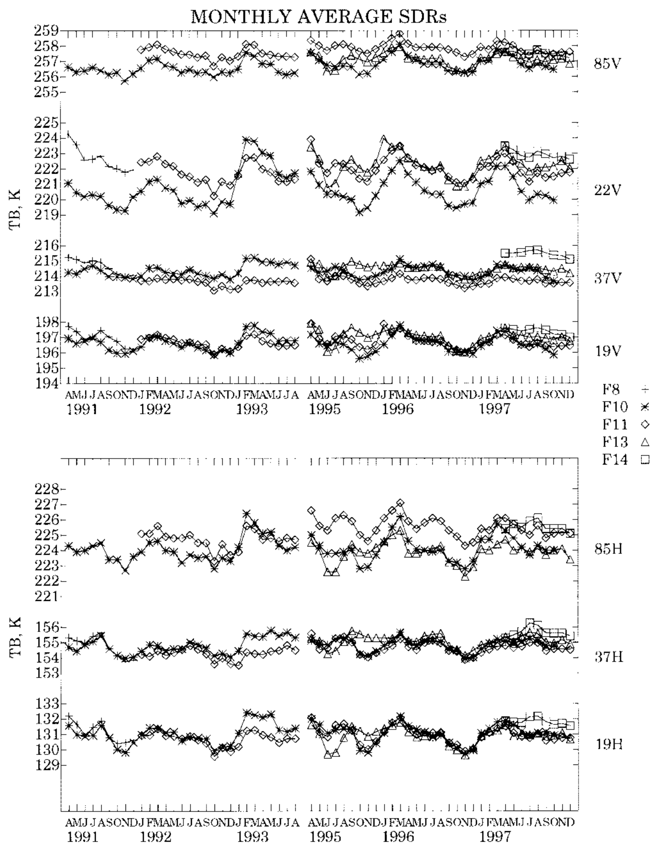

Fig. 8. Monthly averaged, nonprecipitating, ocean SDR's for F8, F10, F11, F13, and F14, vertically polarized (upper panel) and horizontally polarized channels (lower panel), 1991–1997.

of comparison only, the data have been normalized to 53.3° using the coefficients of the EIA term appearing in the model fit to the 1992 F-10 monthly average temperatures.[3] The F-10 model fit was used for all SSM/I's since the more eccentric F-10 orbit magnified the oscillation due to EIA variation, resulting in a numerically better estimate for the mean change of brightness temperature with incidence angle.

For a given SSM/I (Fig. 8), there is a high correlation among the monthly averaged brightness temperatures of all channels with the largest month-to-month variability occurring for 22-V, 19-H, and 85-H channels. To quantify the source(s) of these fluctuations, a principal component analysis of the SSM/I-buoy matchup data sets noted earlier was performed, subject to the additional constraint imposed by the rain flag used in the creation of the monthly averages. The first five eigenvectors for the 19-GHz, 22-V, and 37-GHz channels for F-8, F-10, F-11, and F-13 sensors (Table VIII) decrease rapidly, with the smallest value lying essentially at the sensor noise variance. The first eigenvector is highly correlated with the retrieved water vapor (right-hand side, Table VIII), while the second and third vectors show substantial correlation with wind speed and retrieved cloud water [27]. (Higher correlations are in bold.) Significant correlation occurs between the F-10 third eigenvector and the incidence angle, while appreciable correlation occurs between the fourth eigenvector and the air–sea temperature difference. With the exception of the F-10 third eigenvector, the eigenvectors and correlation coefficients show remarkable consistency between the SSM/I's, providing indirect confirmation of a high level of intersensor radiometer performance.

Further evidence that the environmental variations of atmospheric water vapor constitute the primary source of the brightness temperature fluctuations was obtained by computing the sensitivity of the channel brightness temperatures to water vapor for a global set of atmospheres under cloud-free conditions and a mean surface wind speed of 7 m/s. Although the relationship is nonlinear, the mean channel sensitivities to water vapor are approximately 0.7 K/mm (19 V), 1.2 K/mm (19 H), 1.5 K/mm (22 V), 0.5 K/mm (37 V), 0.9 K/mm (37 H), 0.9 K/mm (85 V), and 2.0 K/mm (85 H) for a nominal water vapor mass of 25 mm. An examination of Fig. 8 reveals that these sensitivities are reasonably close to the relative channel-to-channel brightness temperature fluctuations. (The correspondence is not exact due to the influence of modest cloud attenuation passed by the rain filter and the effects of wind speed.) The fact that the fluctuations are greatest for F-10 (especially 22 V) suggests that the spatial-temporal variability of water vapor may be greater for the F-10 orbit and perhaps amplified by the larger range of the F-10 SSM/I EIA.

Note that remarkably good agreement occurs between 19-V, 19-H, and 37-H channels of F-10 and F-11 for 1992 and between the same channels of F-10, F-11, and F-13 for 1996 and of F-10, F-11, F-13, and F-14 for 1997. Much of the agreement is better than 0.2–0.3 K. Reasonably good agreement also occurs for 1995–1996 between F-10 and F-13 at 85 GHz. However, the F-11 85-GHz data appear consistently higher than the corresponding F-10 and F-13 data. The comparisons between F-10 and F-11 22-GHz channels for 1992 indicate that a relatively constant offset can account for the monthly averaged differences. Unfortunately, the situation changes once the 1993 data are included. The 22-GHz F-10, which appears about 1.5 K cooler than the F-11 in 1992 becomes about 1.0 K warmer than F-11 during the first half of 1993. In 1995 and 1996, the 22-GHz F-10 returns to be 1.5 K cooler than F-11. The periodic rapid rise in the brightness temperatures (especially for F-10) during December to February occurs at the onset of the summer season in the Southern Hemisphere and results from the sampling density of the SSM/I, which is heavily weighted toward the Southern Hemisphere.

Comparisons between 22-GHz F-8 and F-10 for the last nine months of 1991 show a relatively constant, large difference of about 3 K. Interestingly, this level of difference does not occur at the other channels. To understand this behavior, the F-8 monthly average brightness temperatures were analyzed prior to April 1991 (Fig. 9) and found to exhibit periodic behavior at 22 GHz, consistent but reduced with that observed in F-10. Thus, although we obviously do not have F-10 data during the earlier F-8 period, it is likely that the fluctuations of the F-10 monthly averages would not have been consistently lower than the F-8 averages over a multiannual period (as discussed in the next section).

[3] The derived average change of F-10 brightness temperature with incidence angle: 2.2 K/deg at 19 V; 0.5 K/deg at 19 H; 2.1 K/deg at 22 V; 1.9 K/deg at 37 V; 0.5 K/deg at 37 H; 1.0 K/deg at 85 V; and 1.1 K/deg at 85 H.

TABLE VIII
PRINCIPAL COMPONENT ANALYSIS OF SSM/I-BUOY MATCHUP AND CORRELATION WITH ENVIRONMENTAL PARAMETERS

		Channels					Correlation Coefficients				
F-08 (43064 Samples)											
Eigen-Vector	**Eigen-Value**	**19V**	**19H**	**22V**	**37V**	**37H**	**Ws**	**Mv**	**Mc**	**(T_{air}-T_{sea})**	**EIA**
1	891.0	0.36	0.53	0.63	0.23	0.36	-0.13	**0.97**	0.09	0.33	-0.06
2	29.9	-0.16	0.15	-0.54	0.13	0.79	**0.60**	-0.14	**0.59**	-0.09	0.04
3	3.1	-0.12	-0.70	0.31	0.59	0.22	**-0.53**	0.02	**0.57**	0.11	0.08
4	1.9	-0.72	0.00	0.45	-0.47	0.24	0.16	0.05	-0.27	**0.38**	-0.05
5	0.3	0.55	-0.45	0.08	-0.60	0.36	0.26	-0.10	-0.01	-0.20	0.00
F-10 (94336 Samples)											
Eigen-Vector	**Eigen-Value**	**19V**	**19H**	**22V**	**37V**	**37H**	**Ws**	**Mv**	**Mc**	**(T_{air}-T_{sea})**	**EIA**
1	930.1	0.36	0.54	0.63	0.23	0.36	-0.14	**0.97**	0.15	0.34	0.04
2	26.0	-0.16	0.18	-0.56	0.12	0.79	**0.60**	-0.12	**0.55**	-0.12	-0.06
3	3.5	0.27	-0.59	0.02	0.75	0.09	**-0.46**	-0.02	**0.55**	-0.04	**0.53**
4	2.1	-0.71	-0.33	0.53	-0.06	0.31	-0.17	0.07	0.11	**0.36**	-0.18
5	0.4	0.51	-0.47	0.11	-0.60	0.38	0.31	-0.09	-0.07	-0.22	0.14
F-11 (72438 Samples)											
Eigen-Vector	**Eigen-Value**	**19V**	**19H**	**22V**	**37V**	**37H**	**Ws**	**Mv**	**Mc**	**(T_{air}-T_{sea})**	**EIA**
1	903.5	0.36	0.54	0.63	0.23	0.36	-0.15	**0.97**	-0.13	0.29	-0.01
2	28.1	-0.16	0.15	-0.55	0.15	0.79	**0.59**	-0.13	**0.60**	-0.16	0.04
3	2.9	-0.08	-0.68	0.28	0.64	0.20	**-0.57**	0.04	**0.56**	0.10	0.07
4	1.9	-0.75	-0.04	0.46	-0.41	0.26	0.14	0.05	0.17	**0.35**	-0.10
5	0.3	0.53	-0.48	0.10	-0.58	0.37	0.26	-0.11	0.06	-0.27	0.04
F-13 (57986 Samples)											
Eigen-Vector	**Eigen-Value**	**19V**	**19H**	**22V**	**37V**	**37H**	**Ws**	**Mv**	**Mc**	**(T_{air}-T_{sea})**	**EIA**
1	852.2	0.36	0.53	0.63	0.23	0.37	-0.13	**0.97**	-0.04	0.28	0.09
2	26.1	-0.17	0.15	-0.55	0.14	0.79	**0.59**	-0.14	**0.62**	-0.11	0.09
3	2.8	-0.12	-0.68	0.30	0.63	0.20	**-0.58**	0.06	**0.52**	0.12	0.01
4	1.9	-0.74	-0.01	0.45	-0.45	0.23	0.14	0.08	-0.25	**0.36**	-0.12
5	0.3	0.53	-0.48	0.10	-0.59	0.38	0.24	-0.07	0.01	-0.23	0.03
F-14 (9773 Samples)											
Eigen-Vector	**Eigen-Value**	**19V**	**19H**	**22V**	**37V**	**37H**	**Ws**	**Mv**	**Mc**	**(T_{air}-T_{sea})**	**EIA**
1	826.6	0.37	0.54	0.61	0.24	0.38	-0.11	**0.97**	-0.12	-0.25	0.07
2	21.9	-0.21	0.13	-0.53	0.13	0.80	**0.55**	-0.11	**0.62**	0.03	0.01
3	2.6	0.12	-0.66	0.16	0.71	0.13	**-0.60**	0.01	**0.53**	-0.16	0.14
4	1.7	-0.69	-0.23	0.56	-0.27	0.27	0.07	0.06	-0.23	**0.35**	-0.01
5	0.3	0.57	-0.44	0.06	-0.59	0.35	0.28	-0.10	0.01	-0.24	-0.01

Note the presence of a small, somewhat linear, upward trend of the interannual peaks of the F-08 brightness temperatures, especially 22 V and 85 H, in Fig. 9. At 22 V, the net drift between 1988 and 1991 is approximately 2 K. We examined this trend in terms of possible long-term sensor component degradation or drifts. The possibility that the trend may be due to an anomalous (>100 MHz) drift in the local oscillator frequency was ruled out after computations showed that the maximum change in 22-V brightness temperature for a large 200-MHz drift was less than 0.6 K. Also, the possibility that a long-term degradation in the emissivity of the warm-load calibration target would cause the 2-K drift seems unlikely since a decrease in the emissivity would result in a higher surface reflectivity and a corresponding increase in the reflected instrument noise temperature that is typically larger than the thermometric temperature of the warm load. This, in turn, would lower the radiometer gain slope (K/Count) producing a negative drift in the 22-V brightness temperatures.

Finally, we assessed the potential thermal emissions contributions of the reflector. The SSM/I reflector consists of a uniform 0.125 in a graphite/epoxy laminate shell with the front surface metallized with a 5000 Angstrom, vacuum-deposited aluminum. Specular computations were made for a layered medium, which show that the surface vertical and horizontal emissivities are approximately 0.0012 and 0.0011 at 19 and 22 GHz, 0.0014 and 0.0013 at 37 GHz, and 0.0020 and 0.0018 at 85.5 GHz. (We have doubled the specular emissivities to account for the surface roughness effects.) Using worst-case orbit conditions, the maximum reflector temperature is estimated to be less than 50 °C. To explain a 2-K drift at 22 V, the reflector emissivity would have to increase to an extremely large value (0.0194) an order of magnitude increase over the estimated value. Assuming this to be the case, the effect should be even larger in the 37-V brightness temperatures. An examination of Fig. 9 shows that considerably less drift, about 1 K, occurs at 37 V. Thus, it appears that the 2-K drift

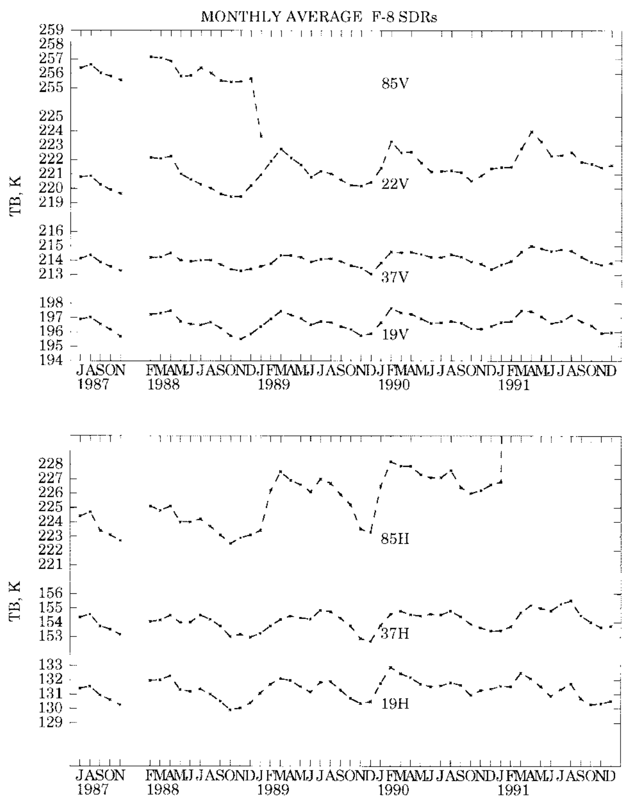

Fig. 9. Monthly averaged, nonprecipitating, ocean SDR's for F8, vertically polarized (upper panel) and horizontally polarized channels (lower panel), 1987–1991.

is due to long-term interannual variability of water vapor over the ocean, as weighted by the SSM/I sampling density.

IV. Distributions of Brightness Temperatures

To gain insight into the intersensor comparisons not offered by the monthly mean brightness temperature, we investigated the empirical statistical distribution functions associated with all periods of SSM/I data noted earlier. This approach not only permits intersensor comparisons over a wide range of conditions, but allows comparisons of data taken over noncoincident time periods. The number of months of SSM/I data used in the construction of the distribution function was 52 for F-8, 60 for F-10, 53 for F-11, 33 for F-13, and nine for F-14. To avoid scan edge contamination, a single pixel near the center of the scan, (i.e., position 33 for the low channels and position 65 for 85 GHz) was selected with both ascending and descending passes included. The total number of samples per channel was approximately 1.1×10^7 for F-8 , 1.1×10^7 for F-10, 1.0×10^7 for F-11, and 7×10^6 for F-13. The distributions were normalized to unit energies in a 0.25-K quantization interval and referenced to a common 53.3° EIA using the coefficients of the EIA model derived from Fig. 7.

The joint distribution functions of rain-filtered ocean pixels were constructed for each year of data for the following four pairs of channels: (19 V, 19 H), (19 H, 22 V), (37 V, 37 H), and (85 V, 85 H). The rationale for selecting these channels was to allow the flexibility to analyze both TDR- and SDR-based distributions and evaluate the impact of the variable APC coefficients. Also, these pairs of channels have the same spatial resolution, share common receiver elements (except for 19 H and 22 V), and have nearly the same feedhorn spillover loss. Higher dimensional distribution functions are of interest, however, they were not viewed as offering appreciably more information about the sensor.

Surface plots of the F-13 joint distribution functions for the entire F-13 period (Fig. 10) show the full range of brightness temperatures for a given frequency pair. Note the high correlation and low rms differences between the 19-, 37-, and 85-GHz polarizations as well as between 22 V and 19 H, indicative of the effectiveness of the rain filter and the restriction to ocean surface observations. Fig. 11 presents the one-dimensional (1-D) projections of the joint SDR distributions (i.e., with the sensor-specific APC coefficients) for all channels. The distributions exhibit similar structures, displaying characteristic signatures corresponding to the natural variabilities in atmospheric water vapor, ocean wind speed, and cloud liquid water weighted by the SSM/I sampling density.

The distribution signatures (Fig. 11) are helpful in identifying anomalous sensor performance, as suggested by the departure of the F-8 85-GHz distributions from those of F-10, F-11, and F-13. This is probably due to the inclusion of a small fraction of data during the period when these channels were starting to degrade. (The 85-V channel started to degrade in October 1987, while the 85-H degradation started in January 1989.) Note the anomalous behavior of the F-8 37-V distribution in the vicinity of the peak value. Although we have no information to suggest otherwise, this behavior raises suspicions regarding potential channel degradations. The best agreement occurs for the 19-H channels, while the largest differences (ignoring the 85-GHz channels) occur at 22 GHz. Relatively large offsets from the F-8 distributions appear for most of the F-13 channels. The F-11 22-V and 85-GHz channels also require large offsets, while for F-10, the 37-H channel displays a large offset.

An analysis was conducted of the normalized distributions to determine the "optimum" linear transformation of the SDR abscissas plus offsets that minimize the variance between the F-8 distribution and the corresponding distributions from all other SSM/I's. The motivation for referencing the offsets to F-8 was driven by the extensive geophysical retrieval algorithm development of the F-8 cal/val program and the desire to use these algorithms for all SSM/I's through sensor-to-sensor corrections. Therefore, for the general case of an n-dimensional vector $\boldsymbol{T}$, the $n \times n$ transformation matrix $\boldsymbol{A}$ and offset vector $\boldsymbol{B}$ for channel n are determined by minimizing the quantity ϵ

$$\epsilon^2(\underline{\underline{A}}, \vec{B}) = \int dT \cdots dT_n [\eta_{\mathrm{F8}}(\vec{T}) - |\underline{\underline{A}}| \eta_x(\underline{\underline{A}}\vec{T} + B)]^2 \quad (5)$$

where $\eta_{\mathrm{F8}}(\boldsymbol{T})$ is the F-8 temperature distribution and $\boldsymbol{A}\eta_x(\boldsymbol{AT} + \boldsymbol{B})$ is the distribution of the same channel for sensor x. In the 1-D case, (a, b) are selected to minimize the difference

$$\epsilon^2(a, b) = \int dT [\eta_{\mathrm{F8}}(T) - |a| \eta_x(aT + b)]^2. \quad (6)$$

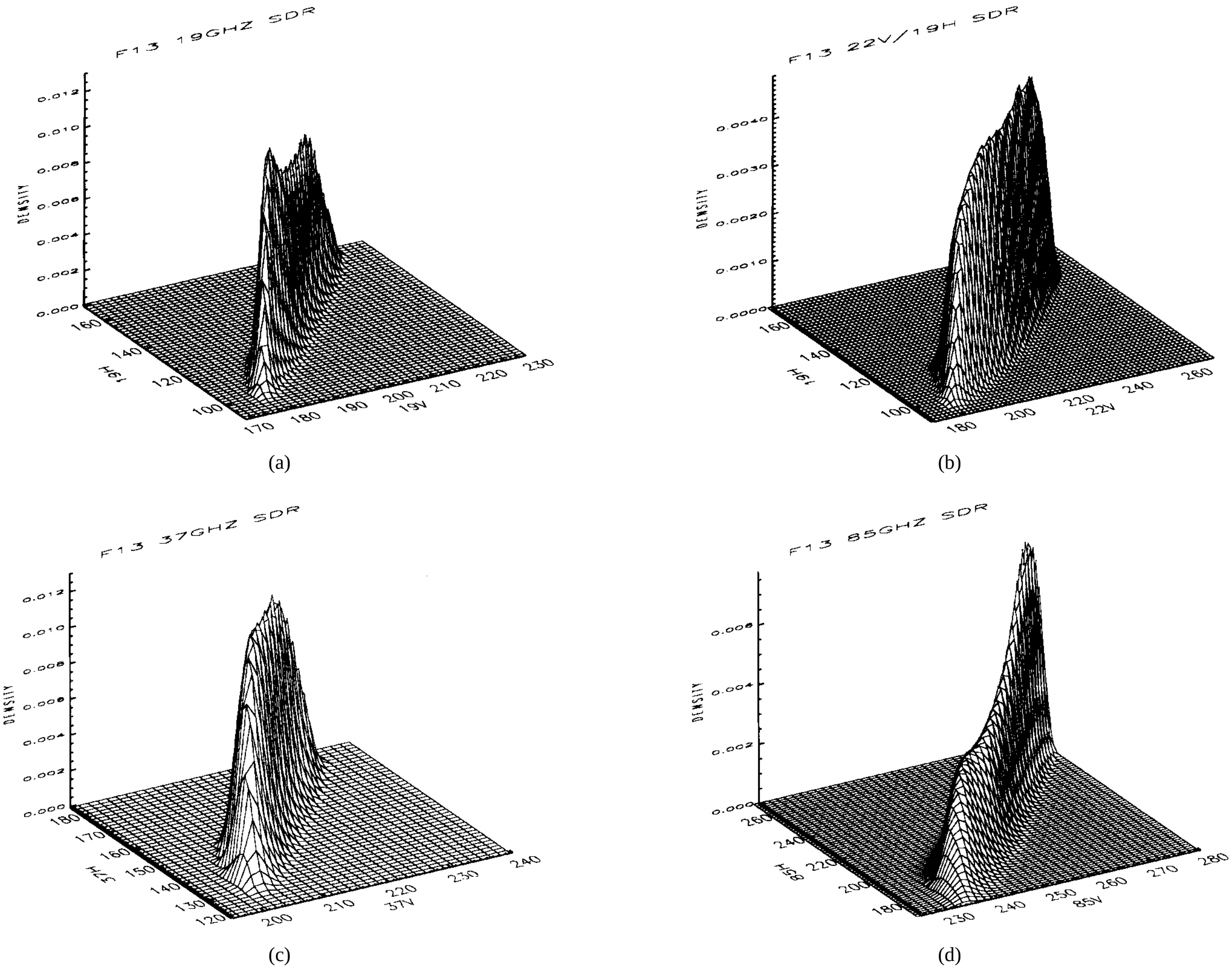

Fig. 10. Joint distribution functions for 30 months of F13 data, (a) (19 V, 19 H), (b) (19 H, 22 V), (c) (37 V, 37 H), and (d) (85 V, 85 H).

This is equivalent to solving for the transformation and offsets, which produce the maximum correlation between the associated distributions.

The results of extending the analyses using paired brightness temperature two-dimensional (2-D) formulations noted above revealed that nonphysical slopes and offsets arose in many cases and exhibited essentially no improvement in variance reduction over cases in which only an offset was used. This situation is traceable to the small difference in information content between the distributions; i.e., the distributions are sufficiently similar so that a single offset is sufficient to remove the major differences between the distributions.

This point may be further elucidated by examining the *empirical characteristic function*, ϕ, for the 1-D distribution of variable T for sensor x, which is defined as the Fourier transform

$$\varphi_x(u) = \int e^{i2\pi uT} \eta_x(T)\, dT. \tag{7}$$

Therefore, the characteristic function of an "offset" distribution $\eta'_x(T) = |a|\eta_x(aT+b)$ becomes

$$\varphi'_x(u) = \int e^{i2\pi uT}[|a|\eta_x(aT+b)]\, dT. \tag{8}$$

Substituting $T' = aT + b$ yields

$$\begin{aligned}\varphi'_x(u) &= e^{-i2\pi u(b/a)} \int e^{i2\pi(u/a)T'} \eta_x(T')\, dT' \\ &= e^{-i2\pi u(b/a)} \varphi_x\left(\frac{u}{a}\right)\end{aligned} \tag{9}$$

and

$$|\varphi'_x(u)_x| = \left|\varphi_x\left(\frac{u}{a}\right)\right|. \tag{10}$$

That is, the magnitude of the characteristic function of the transformed distribution is only affected by the multiplicative factor a. The characteristic functions of the 22-V channel distributions (Fig. 12) pass as expected through a common point at the origin and show that a is very near unity, indicating that the majority of the differences between the original distributions may be minimized by adjusting only the offset factor b.

Table IX presents the optimum channel offsets needed to bring the SDR-based distributions into alignment with those of F-8 and quantifies the descriptions of Fig. 11. Relatively large offsets are required for F-11, F-13, and F-14 for 22 GHz, F-13 and F-14 for 37 GHz, and F-11 and F-14 for 85 GHz. On the other hand, the large 3-K offset observed earlier between

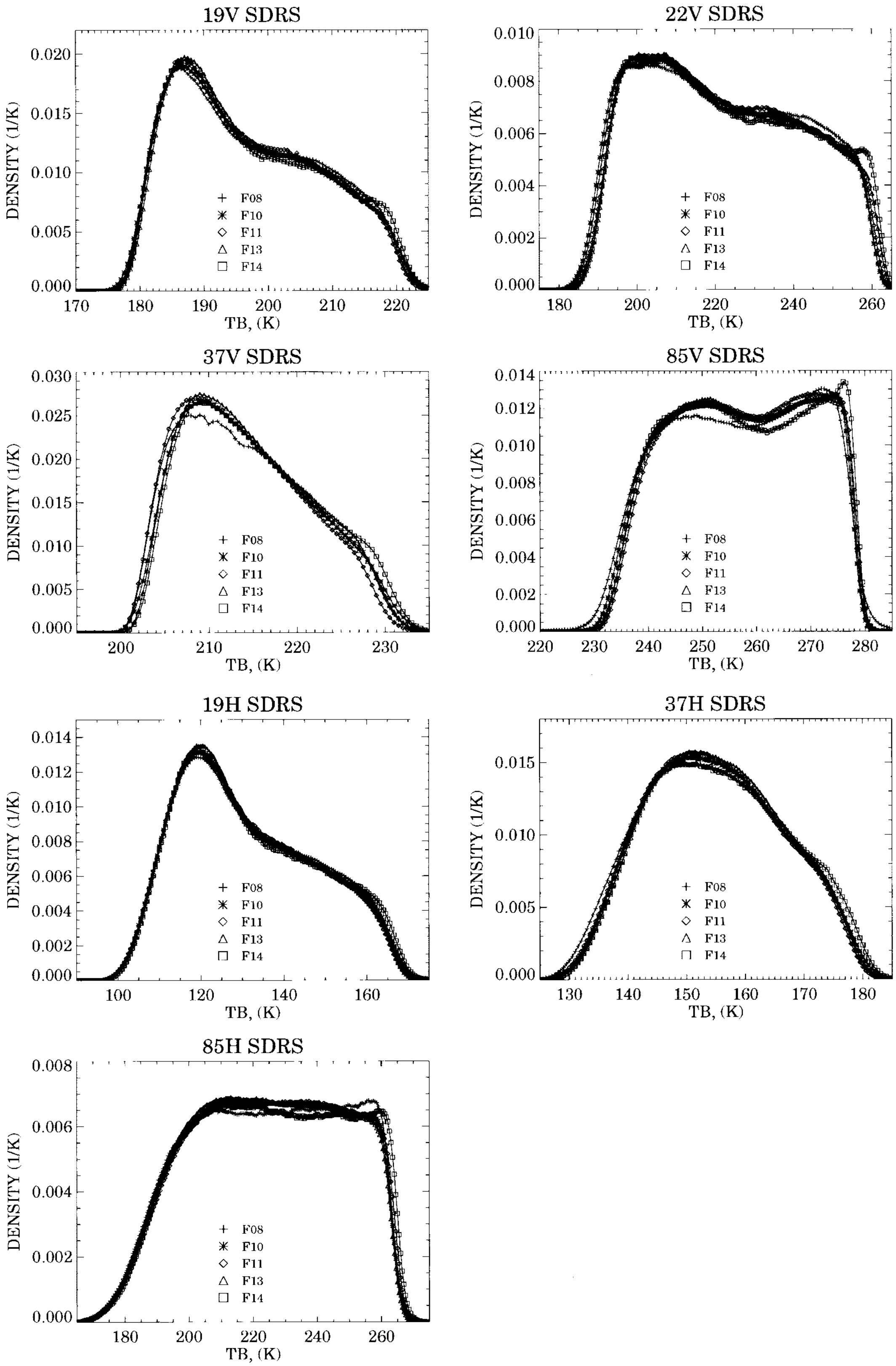

Fig. 11. Distributions of brightness temperature (SDR's) for nonprecipitating, ocean pixels, all channels, F8, F10, F11, F13, and F14, 1991–1997.

F-8 and F-10 22-GHz monthly means (Fig. 8) is reduced to a 0.35-K offset when analyzed in terms of distributions (including all data sets).

For comparison, Fig. 13 presents the 1-D TDR-based distributions corresponding to the SDR distribution of Fig. 11. Note the substantial improvement in agreement for many channels. Table IX(b) presents the channel offsets necessary to bring the TDR-based distributions into alignment with F-8. Remarkably, most of the large offsets noted above for the SDR-based distributions are greatly reduced, especially

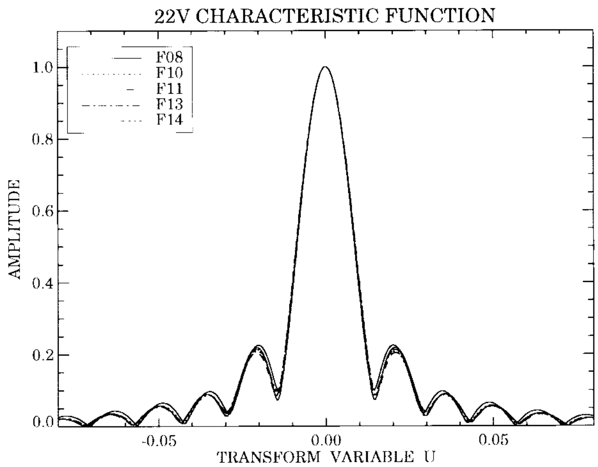

Fig. 12. Magnitude of characteristic functions of 22-GHz, vertically polarized SSM/I brightness temperature distribution.

TABLE IX
OFFSET FACTORS FOR OPTIMIZATION OF F8, F10, AND F11 BRIGHTNESS TEMPERATURE DISTRIBUTIONS WITH RESPECT TO F8: (a) SDR-BASED DISTRIBUTIONS (SENSOR-SPECIFIC APC COEFFICIENTS AND (b) TDR-BASED DISTRIBUTIONS (NO APC APPLIED)

Channel	F-10	F-11	F-13	F-14
19V	-0.10	-0.30	-0.65	-0.45
19H	-0.05	0.05	-0.10	-0.30
22V	0.35	-0.75	-1.35	-1.60
37V	-0.40	0.10	-0.60	-1.00
37H	-0.70	-0.40	-0.95	-1.20
85V	-0.25	-1.05	-0.65	-1.20
85H	0.05	-1.00	0.35	-1.60

(a)

Channel	F-10	F-11	F-13	F-14
19V	-0.15	-0.35	-0.55	-0.05
19H	-0.35	0.10	-0.25	0.05
22V	0.20	0.10	0.00	0.30
37V	-0.30	-0.25	-0.30	-0.30
37H	-0.30	0.15	-0.05	-0.10
85V	0.25	-0.40	-0.20	-0.35
85H	-0.15	-0.45	-0.25	-0.45

(b)

for the 22-V channels. However, not all SDR-based offsets have reductions, e.g., the 19-GHz channels (except for F-13 19 V) and the F-10 85-GHz channels, although the differences between these offsets are typically less than 0.15 K.

The largest offset for the TDR-based distributions occurs with F-13 19 V. In view of the uncertainty in the EIA noted earlier, $\pm 0.1^{\circ}$, the process of normalizing the distributions to 53.3° could have introduced an error for the F-13. Assuming this to be true, a 0.1 (EIA increase would result in the F-13 TDR-based offsets of -0.35, -0.20, 0.20, -0.10, 0.00, -0.10, and -0.15 K, bringing all TDR-based offsets to levels less than 0.35 K, except the 0.45-K offset for F-11 and F-14 85 H. Fig. 14 shows the effect of including the offsets on the 22-V SDR- and TDR-based distributions.

V. DISCUSSION AND CONCLUSIONS

The cal/val results reported herein demonstrate that individually the SSM/I's are remarkably stable microwave radiometers providing high-quality imagery of important geophysical parameters, such as sea surface wind speed, integrated water vapor over ocean, and sea ice concentration. The objective of this study was to quantify the incremental brightness temperature differences to which the SSM/I's could be intercalibrated, thus establishing the "noise floor" for intercomparisons. The approach was to examine individual sensor-specific components, orbital configuration, and systematic relative errors that contribute to the total system calibration. The statistical analyses required to assess the system component errors have inherent limitations themselves. Therefore, the "noise floor" to which we can justifiably compare individual SSM/I sensors is a combination of actual sensor calibration differences and comparison methodology.

The study began with analysis of preflight thermal-vacuum calibration measurements of the individual sensors over the predicted orbital environmental conditions and established the instrument stability (average NEDT: 19 V, 0.44; 19 H, 0.42; 22 V, 0.58; 37 V, 0.33; 37 H, 0.34; 85 V, 0.57; 85 H, 0.52) and calibration accuracy (1–2 K). Early orbit analysis confirmed the preflight radiometer sensitivities and the high-quality uniformity and repeatability of the instrument calibration. *The excellent on-orbit calibration data show that preflight adjustment of calibration coefficients based on laboratory data may not be good practice, given that the original SSM/I preflight thermal vacuum data contained artifacts due to incomplete radiometric coupling between the feedhorn and cold calibration target.*

Detailed studies of the image uniformity across the scan have shown the presence of a systematic left-to-right scan asymmetry associated with a pixel-dependent energy loss (approximately 1–2 K, depending on the channel), most notable at the end of scan, and traceable to the spacecraft (start of scan) and GSS-B (end-of-scan) intrusions into the SSM/I FOV. Although the effects of the intrusion may be corrected to first order in terms of a pixel-dependent spillover correction, as verified with the removal of the observed along-scan ocean wind speed retrieved bias error, *we strongly recommend that possible influences of the spacecraft and FOV intrusions on the antenna pattern be quantified prior to launch.* Clearly, the effects of the FOV intrusion become important when making fine intercomparisons or resolving geophysical features exhibiting a small range of brightness temperatures.

The SSM/I operates on an extremely stable spacecraft platform, as evidenced by the repeatability of the SSM/I spin axis alignment coefficients that bring the geolocation errors to within 6–7 km. (The DMSP spacecraft pointing stability is approximately 0.01° (1 sigma) per axis in the precision mode and 0.12° per axis in the basic or backup mode.) Verification of the SSM/I alignment coefficients and associated EIA (to within approximately 0.1°) was obtained through an analysis of the rms wind speed retrieval error and its dependence on the incidence angle.

A study of the 1992 monthly average F-10 brightness temperatures of rain-filtered ocean scenes in terms of ascending and descending passes revealed the presence of large oscillating patterns and a small, slowly varying trend. These behaviors were found to be highly correlated with the oscillating monthly

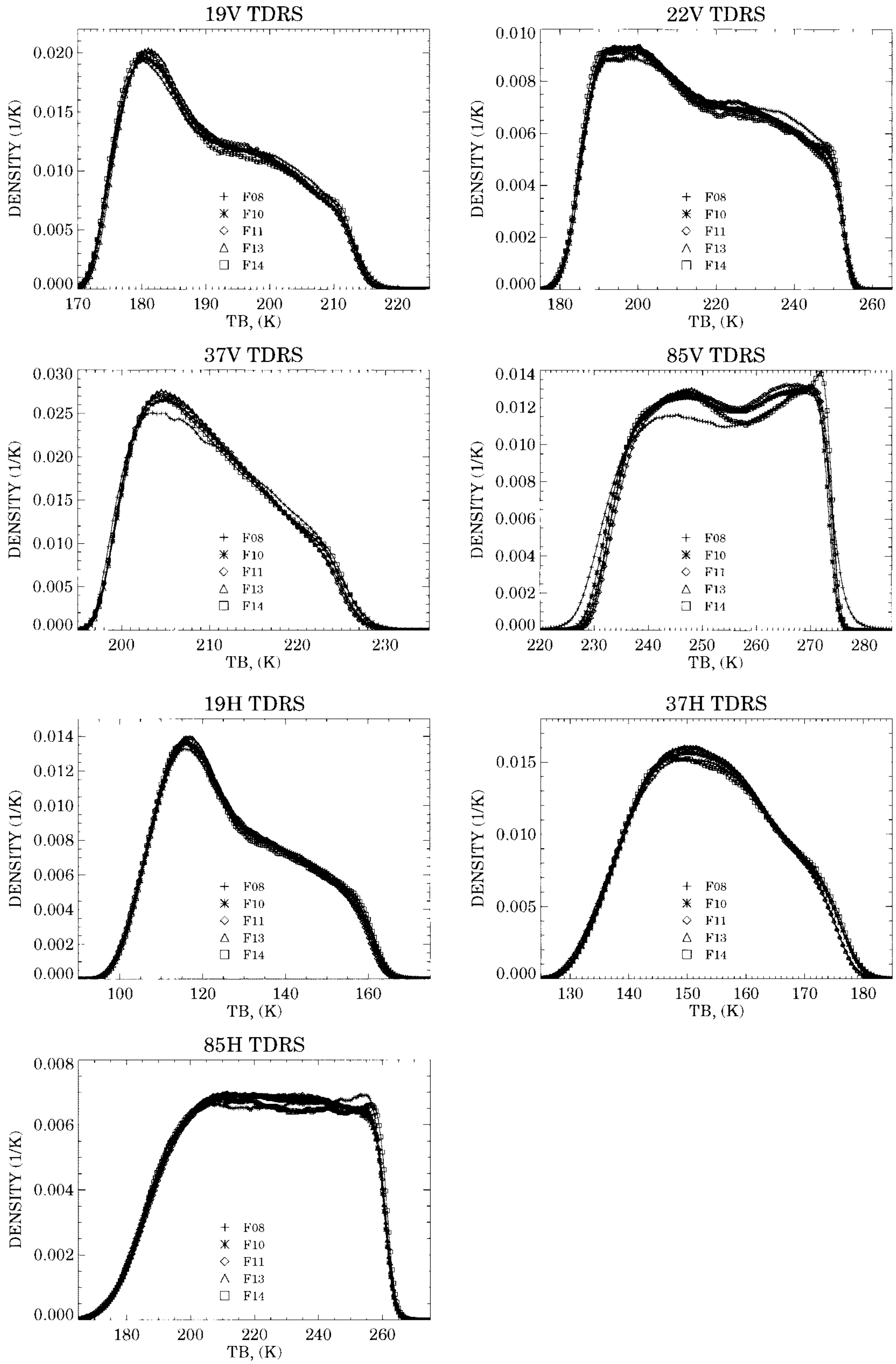

Fig. 13. Distributions of antenna temperature (TDR's) for nonprecipitating, ocean pixels, all channels, F8, F10, F11, F13, and F-14, 1991–1997.

average EIA and a slowly varying monthly average sea surface temperature (weighted by SSM/I sampling density), which we believe is a surrogate for atmospheric water vapor. The residual rms errors associated with fitting a linear model of the EIA and sea surface temperature to the F-10 monthly average temperatures were found to be less than 0.26 K for the 19- and 37-GHz channels and less than 0.37 K for the 22- and 85-GHz channels. A similar analysis of the 1992 F-11 brightness temperatures yielded essentially the same rms errors, suggesting error limits for the intersensor comparisons.

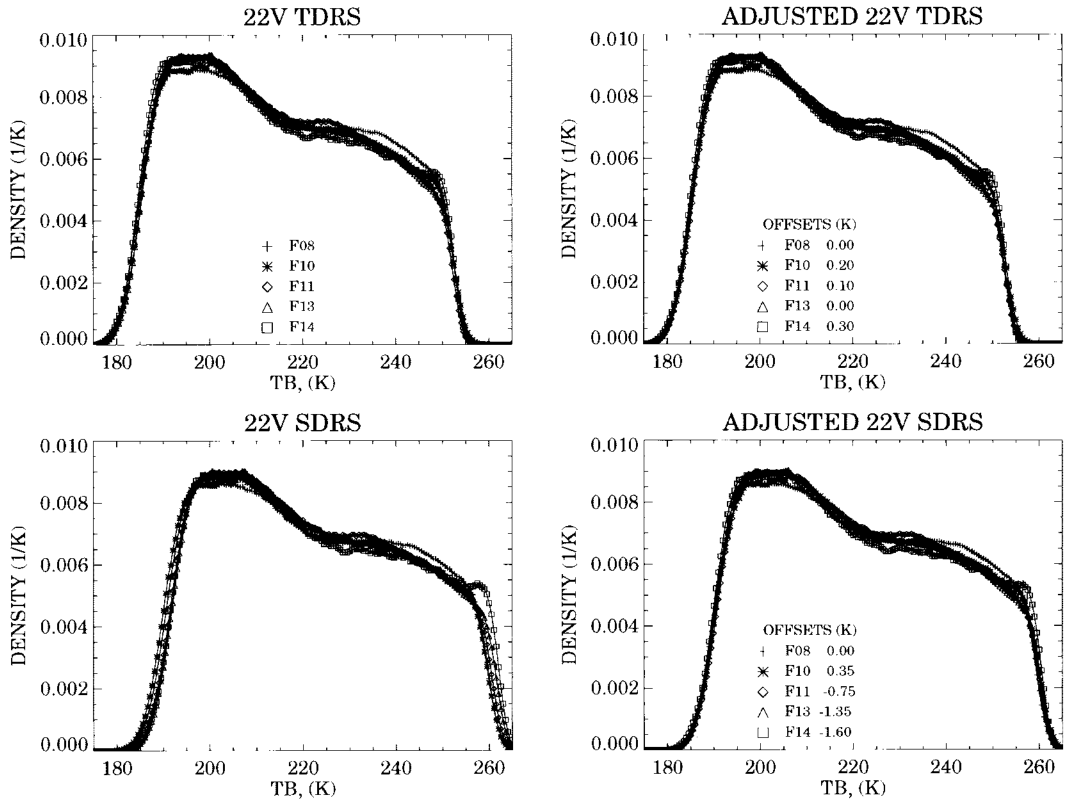

Fig. 14. Distributions of 22-V temperatures for F8, F10, F11, F13, and F-14, 1991–1997: (a) TDR's, (b) TDR's with offsets applied, (c) SDR's, and (d) SDR's with offsets.

An extensive data processing effort was undertaken to compute the monthly average rain-filtered ocean brightness temperatures for F-8, F-10, F-11, and F-13 SSM/I's for the period September 1993–March 1995. Using the EIA coefficients derived for the above model fit to the 1992 F-10, the monthly average brightness temperatures (with the sensor-specific APC) were normalized to a common 53.30 incidence angle.

For a given SSM/I, high correlation exits between all channels, with the largest month-to-month variability occurring for the 22-V, 19-H, and 85-H channels, consistent with the natural variability of atmospheric water vapor passed by the rain filter. The large periodic increase in the monthly averages were observed to occur during the December–February period, reflecting the onset of summer and the greater sampling density of SSM/I data in the Southern Hemisphere. These peaks also exhibited varying amplitude from year to year. For a given channel, the SSM/I's exhibit reasonably constant differences on an annual basis, suggesting the possibility of constant intersensor calibration offsets. However, these differences were observed to change significantly from year to year in concert with the large December–February changes. This situation was most evident when the above model was fitted to F-10 for the period 1992–1993. Relatively large rms residual errors arose, indicating that the model incorporating the incidence angle and sea temperature was unable to account for the interannual fluctuations. On the other hand, fitting the model separately to 1992 and 1993 yielded comparable results.

When the sensor-specific APC was changed to that of F-8, differences in the monthly averages were reduced for the low-frequency channels of F-10 and F-11 for the periods 1992 and 1995–1996. Unfortunately, the differences increased for 1993.

Thus, the interpretation of sensor-to-sensor differences based solely on the monthly mean temperatures must be viewed as inconclusive, and the adjustment of temperatures ill-advised. However, these data indicate that the agreement between the SSM/I's for limited periods is remarkably consistent, such that computing regression coefficients between sensors for specialized applications requiring "data consistency" over short periods is probably justified. Multiyear regressions are not recommended, as there are clearly longer term seasonal and sensor related effects that require corrections achievable only in *ad hoc* fashion when using mean temperatures alone.

To increase the range of brightness temperatures for intersensor comparisons, the SSM/I data processing efforts were expanded to include the construction of statistical distribution functions of rain-filtered ocean brightness temperatures for all periods of data. Both TDR and SDR distributions were created for a single pixel located near the center of scan (position 33 for the low channels and 65 for the 85-GHz channels), including both ascending and descending passes within $\pm 60°$ latitude. For a given channel, the distributions were observed to have similar characteristic structures associated with the range of natural variability of atmospheric water vapor, ocean wind speeds, and cloud liquid water passed by the rain filter.

The distributions were analyzed in terms of an optimum offset in brightness temperature that maximizes the cross correlation of the F-10, F-11, and F-13 densities with the F-8 density. A large 3-K monthly mean offset observed between the F-8 and F-10 22-GHz channels in 1991 was reduced to 0.35 K when analyzed in terms of distribution functions when all data sets were included. This result suggests the possibility that systematic orbitally induced sampling differences may be the cause of the offsets for the nine months of 1991. Furthermore, Table IX shows that the offsets needed to match the TDR-based F-10, F-11, and F-13 distributions were on the order of 0.2–0.35 K, with the exception of the F-13 19 V (−0.55 K) and F-11 and F-14 85-H (−0.45 K) channels. It is noteworthy that the TDR offsets (Table IX, with the exception of F-13 19 V) are approximately the same magnitude as the residual rms errors associated with the above model fit to the 1992 data (Table VIII). *Due to the influence of long-term, pseudorandom, spatial-temporal environmental fluctuations, which we have tried to minimize using distribution functions, we feel that the TDR-based offsets should be interpreted in terms of basic uncertainties of the methodology and not in terms of real sensor differences. As such, the SSM/I's are believed to be intercalibrated at the TDR level to within the uncertainties of the methodology, namely, 0.25–0.35 K for the low-frequency channels and 0.45 K for the 85-GHz channels*. The differences of the low channels are about a factor of two less than the intercalibration offsets noted by Wentz [23].

In contrast, the offsets needed to match the SDR-based (sensor-specific APC) F-10, F-11, and F-13 distributions [Table IX(a)] were significantly larger for many channels. For example, the offsets needed for the 22-GHz F-11, F-13, and F-14 channels are −0.75, −1.35, and −1.60 K, respectively, while an offset of −0.95 and −1.20 K is needed for F-13 and F-14 37 H. These singularly large offsets are above the noise level of the 0.25–0.35 K mentioned above, and they are correlated with the effects of the sensor-specific APC noted in Table III(a) for a highly polarized ocean scene. *The magnitude of the SDR offsets underscores the importance of obtaining a full and accurate characterization of the feedhorn spillover loss and cross-polarization coupling*. Long-term studies of environmental parameters derived from algorithms using the channels that have large differences may partially alleviate the situation by employing one APC for those channels, say, the F-8 APC, for consistency across sensors.

We have demonstrated the merits of the SSM/I TDR and SDR distribution functions as being a visual signature of microwave brightness temperature at a specified frequency, a qualitative technique for identification of sensor malfunction, or a quantitative mechanism for resolving calibration differences. At this point, we interpret the distribution offsets as the noise floor of the SSM/I instruments. They have components of calibration, APC, and orbital and environmental errors that are not resolvable in the retrospective view.

Reducing the noise floor to O (0.1 K) for future sensors will require highly detailed information about the sensor (e.g., accurate APC, oscillator frequency and passband stability, and sensor-to-spacecraft alignment offsets), improved orbital elements, and spacecraft attitude information. Further sampling will have to be optimized for interpolation of data, information content of scene, and validation of measurements. With these improvements comes the opportunity to use long-term space-based sensors to resolve incremental environmental changes for climatological applications, development of accurate forward radiative transfer models, and direct radiance assimilation in numerical weather prediction models.

Acknowledgment

The authors thank A. Uliana and B. Gardiner for their relentless efforts in processing the SSM/I data and assistance with graphical results. The exceptional ground support and operational processing of all on-orbit SSM/I's during the Early Orbit Periods at Fleet Numerical Meteorology and Oceanography Center is gratefully acknowledged as well as continued access to the SSM/I data. They thank J. Peirce (Hughes Aircraft Co., SSM/I Project Engineer) for providing historical insight, photographs, and the SSM/I thermal vacuum calibration data. Dr. F. Weng (NOAA/NESDIS) supplied the NCDC sea surface temperature data.

Finally, they would like to dedicate this work to the memory of their friend and colleague, Dr. J. P. Hollinger, whose own early and continued dedication to the DMSP SSM/I program was instrumental to its success.

References

[1] J. P. Hollinger, Ed., *DMSP Special Sensor Microwave Imager Calibration/Validation*, vol. I, Naval Res. Lab., Washington, DC, Final Rep., July, 1989.

[2] J. P. Hollinger, J. L. Peirce, and G. A. Poe, "SSM/I instrument evaluation," *IEEE Trans. Geosci. Remote Sensing*, vol. 28, pp. 781–790, July 1990.

[3] J. P. Hollinger, Ed., *DMSP Special Sensor Microwave Imager Calibration/Validation*, vol. II, Naval Res. Lab., Washington, DC, Final Rep., May 1991.

[4] M. C. Colton, "DMSP special sensor microwave imager (SSM/I) processing at the Fleet Numerical Oceanography Center: Operational status, applications and plans," in *Proc. AMS 6th Conf. Satellite Meteorol. Oceanogr.*, Jan. 5–10, 1992, pp. 453–456.

[5] J. P. Hollinger, D. K. Conway, R. W. Conway, and J. Spangler, "Calibration/validation of SSM/I 2 on DMSP F-10," Naval Res. Lab., Washington, DC, Final Rep., Sept. 1991.

[6] J. P. Hollinger, "Early orbit report for SSM/I 3 on DMSP F-11," Naval Res. Lab., Washington, DC, Memo., Dec. 1991.

[7] G. A. Poe, E. A. Uliana, M. C. Colton, W. Bercik, and B. Gardiner, "Calibration and validation of DMSP SSM/I F-12: Early orbit period," FNMOC Internal Tech. Rep., Ser. Num. 70/1099, Oct. 1994.

[8] ——,, "Calibration and validation of DMSP SSM/I F-13: Early orbit period," FNMOC Internal Tech. Rep., Ser. Num. 70/763, June 1995.

[9] G. A. Poe, J. Tesmer, J. Cornelius, B. Gardiner, and E. A. Uliana, "Calibration and validation of DMSP SSM/I F-14: Early orbit results and performance of the first three months," FNMOC Internal Tech. Rep., July 1997.

[10] D. L. Randel *et al.*, "A new global water vapor data set," *Bull. Amer. Meteorol. Soc.*, vol. 77, pp. 1233–1246, June 1996.

[11] D. Halpern and F. Wentz "On the problem of measuring interannual wind speed variations using SSM/I data," *Geophys. Res. Lett.*, vol. 21, pp. 193–196, Feb. 1994.

[12] D. Halpern, "ECMWF and SSM/I global surface wind speeds," *J. Atmos. Ocean. Technol.*, vol. 11, pp. 779–788, June 1994

[13] W. Steffan, C. Otto, and K. Jezek, "Comparison of brightness temperatures from SSM/I instruments on the DMSP F08 and F11 satellites for Antarctica and the Greenland ice sheet," *Int. J. Remote Sensing.*, vol. 16, pp. 1223–1229, 1995.

[14] J. Bouten and J. Etcheto, "Consistency of Geosat, SSM/I, and ERS-1 global surface wind speeds—Comparison with *in-situ* data," *J. Atmos. Ocean. Technol.*, vol. 13, pp. 183–197, Feb. 1996.

[15] T. J. Greenwald, G. Stephans, S. Christopher, and T. H. VonderHaar, "Observations of the global characteristics and regional radiative effects of marine cloud liquid water," *J. Climate*, vol. 8, pp. 2928–2945, 1995.

[16] G. Stephens, D. Jackson, and J. Bates, "A comparison of SSM/I and TOVS column water vapor data over the global oceans," *Meteorol. Atmos. Phys.*, vol. 54, pp. 183–201, 1994.
[17] D. Jackson and G. Stephens, "A study of SSM/I derived columnar water vapor over the global oceans," *J. Climate*, vol. 8, pp. 2025–2038, Aug. 1995.
[18] R. Fuhrkop and C. Summer, "SSM/I brightness temperature corrections for incidence angle variations," *J. Atmos. Ocean. Technol.*, vol. 13, pp. 246–254, Feb. 1996.
[19] J. J. Bates, "High frequency variability of special sensor microwave/imager derived wind speed and moisture during an intraseasonal oscillation," *J. Geophys. Res.*, vol. 96, pp. 3411–3423, Feb. 1991.
[20] L. Phalippou, "Variational retrieval of humidity profile, wind speed and cloud liquid water path with the SSM/I: Retrieval for numerical weather prediction," *Quart. J. R. Meteorol. Soc.*, vol. 122, pp. 327–355, Jan. 1996.
[21] R. Atlas, R. Hoffman, S. Bloom, J. Jusem, and J. Ardizzone, "A multiyear global surface wind velocity dataset using SSM/I wind observations, *Bull. AMS*, vol. 77, pp. 869–881, May 1996.
[22] R. R. Ferraro, F. Weng, N. Grody, and A. Bassist, "An eight-year (1987–1994) time series of rainfall, clouds, water vapor, snow cover, and sea ice derived from SSM/I measurements," *Bull. AMS*, vol. 77, pp. 891–905, May 1996.
[23] F. J. Wentz, *User's Manual SSM/I Antenna Temperature Tapes Revision 1*, RSS Tech. Rep. 120191, Dec. 1991.
[24] A. P. Stogryn, C. T. Butler, and T. J. Bartolac, "Ocean surface wind retrievals from special sensor microwave/imager data with neural networks," *J. Geophys. Res.*, vol. 90, pp. 981–984, 1994.
[25] F. J. Wentz, *Revision 1 Update for SSM/I Geophysical Tapes User's Manual*, RSS Tech. Memo. 040792, Apr. 1992.
[26] *Interface Control Document for DMSP Block 5D2 (S11-S14) Mission Sensor SSM/I*, ICD-2617407, Martin Marietta Astrospace, Princeton, NJ, June 1989.
[27] F. J. Wentz, "Measurement of oceanic wind vector using satellite microwave radiometers," *IEEE Trans. Geosci. Remote Sensing*, vol. 30, pp. 960–972, Sept. 1992.
[28] R. W. Spencer and J. R. Christy, "Precise monitoring of global temperature trends from satellite," *Science*, vol. 246, pp. 1558–1562, 1990.
[29] J. R. Christy, R. W. Spencer, and R. T. McNider, "Reducing noise in the MSU daily lower-tropospheric global temperature dataset," *J. Climate*, vol. 8, pp. 888–896, 1995.
[30] P. Gloerson, W. J. Campbell, D. J. Cavalieri, J. C. Comiso, C. L. Parkinson, and H. J. Zwally, *Arctic and Antarctic Sea Ice, 1978–1987, Satellite Passive-Microwave Observations and Analysis*, NASA Rep. SP-511, 1992, p. 290.
[31] J. Peirce, SSM/I Program Manager, Hughes Aircraft Co., personal communication.

Marie C. Colton (A'90) received the B.A. and M.S. degrees in physical oceanography from Florida Institute of Technology, Melbourne, in 1978 and 1981, respectively, and the Ph.D. degree in physical oceanography from the Naval Postgraduate School, Monterey, CA, in 1989.

She was a Federal Intern at the NASA Headquarters Oceanic Processes Branch in 1979 and in the Geodynamics Branch at NASA Goddard Space Flight Center, Greenbelt, MD, in 1980, where she completed a thesis using Seasat altimeter data to study the Antarctic Circumpolar Current. From 1980 to 1983, she was a fluid systems engineer at NASA Kennedy Space Center, working on the life support systems of space shuttles Columbia and Challenger. From 1983 to 1986, she worked on a ocean modeling research program in the Department of Oceanography, Naval Postgraduate School. At the Naval Research Laboratory, Monterey, from 1986 to 1990, she studied environmental effects on radar backscatter and managed the ground processing software development for the active microwave instruments on the Naval Remote Ocean Sensing Satellite. From 1990 to 1997, she was responsible for the operational processing of the DMSP Special Sensor Microwave Imager at the Fleet Numerical Meteorology and Oceanography Center, Monterey. She is currently the Program Officer for remote sensing at the Office of Naval Research, Arlington, VA, where she manages Navy research efforts in microwave remote sensing.

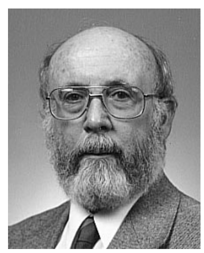

Gene A. Poe (M'91) received the B.A. and M.S. degrees in electrical engineering from the University of California, Berkeley, in 1964 and 1965, respectively.

He has worked in wide-ranging capacities for the major aerospace companies responsible for the development of space-based passive microwave instruments (Aerojet Corp., 1965–1972 and 1989–1993; Hughes Aircraft Co., 1976–1982). His experiences in passive microwave remote sensing include making and analyzing field measurements, developing emissivity models, and participating in the design of space sensors (DMSP SSM/I, SSM/IS, T-2, and NOAA Advanced Microwave Sounding Unit). From 1986 to 1989, he worked at the Space Sensing Branch, Naval Research Laboratory, Washington DC, on microwave radiometric modeling and analysis of SSM/I data. He is currently Chief Scientist of Passive Microwave Sensing in the Remote Sensing Physics Branch, Remote Sensing Division, Naval Research Laboratory.